

Hybrid gradient smoothing technique with discrete shear gap method for shell structures



W. Li ^{a,b,c}, Z.X. Gong ^a, Y.B. Chai ^{a,*}, C. Cheng ^d, T.Y. Li ^{a,b,c}, Q.F. Zhang ^a,
M.S. Wang ^a

^a School of Naval Architecture and Ocean Engineering, Huazhong University of Science and Technology, Wuhan 430074, China

^b Hubei Key Laboratory of Naval Architecture and Ocean Engineering Hydrodynamics, Huazhong University of Science and Technology, Wuhan 430074, China

^c Collaborative Innovation Center for Advanced Ship and Deep-Sea Exploration (CISSE), Shanghai 200240, China

^d Wuhan Ship Development & Design Institute Co. Ltd. (WSDDI), Wuhan 430074, China

ARTICLE INFO

Article history:

Received 29 November 2016

Received in revised form 14 March 2017

Accepted 26 June 2017

Available online 31 July 2017

Keywords:

Gradient smoothing technique (GST)

Numerical method

Discrete shear gap (DSG)

Shell structures

ABSTRACT

In order to enhance the performance of the discrete shear gap technique (DSG) for shell structures, the coupling of hybrid gradient smoothing technique (H-GST) with DSG using triangular elements (HS-DSG3) is presented to solve the governing partial differential equations of shell structures. In the formulation HS-DSG3, we firstly employ the node-based gradient smoothing technique (N-GST) to obtain the node-based smoothed strain field, then a scale factor $\alpha \in [0, 1]$ is used to reconstruct a new strain field which includes both the strain components from standard DGS3 and the strain components from node-based smoothed DSG3 (NS-DSG3). The HS-DSG3 takes advantage of the “overly-soft” NS-DSG3 model and the “overly-stiff” DSG3 model, and has a relatively appropriate stiffness of the continuous system. Therefore, the degree of the solution accuracy can be improved significantly. Several typical benchmark numerical examples have been investigated and it is demonstrated that the present HS-DSG3 can provide better numerical solutions than the original DSG3 for shell structures.

© 2017 Elsevier Ltd. All rights reserved.

1. Introduction

As is known to all, shell structures have been extensively used in various engineering applications including ships, aircraft, industrial buildings and so on. Therefore, how to effectively simulate the behaviors of shell structures is very important in practice and this topic also has attracted many research interests in the past few decades. A shell structure, essentially, can be considered as a plate structure with a curved middle surface. However, the way in which shell structures carry loading is very different from plate structures. The plate structures can usually undergo the loading in the transversal direction which can result in bending behavior, while the shell structures can support the loading in all directions. There are many numerical techniques that can be used to simulate the behaviors of shell structures, such as the finite element method [1], the boundary element method [2], the meshfree method [3,4], the generalized differential quadrature method [5–8] and so on. Among them, the classical finite element method has been demonstrated to be a well-developed and powerful numerical method.

The general shell elements consist of the following three main types [9]: the first kind of shell element is the degenerated shell element which is formulated from the 3D solid theory. The second one is the curved shell element which can be

* Corresponding author.

E-mail address: cybhust@hust.edu.cn (Y.B. Chai).

derived from the general shell theory. The last one is the flat shell element which can be considered as the combination of the membrane element associated with plane elasticity and the plate bending element associated with plate theory. The membrane element handles the membrane effects, while the plate element is used to tackle the bending effects. Since the derivation of detailed governing equations for the previous two categories of shell elements can be very complicated and presents many difficulties, in practice, the flat shell element is the dominating shell element model due to its easy formulation and low computational cost. In this work, we also use the flat shell elements to perform the analyses of shell structures.

In practical application, the displacement formulation based on Reissner–Mindlin theory is very popular due to both computational and physical advantages. These displacement-based shell elements possess fast convergence rate and high accuracy properties. However, for the bending-dominated shell structures, they often result in “overly-stiff” solutions when the shell thickness trends to zero, this is the so-called shear locking issue. As is well-known, the shear locking issue always arises for very thin plates and shells due to the spurious constraining. As a result, the obtained numerical solutions are always unreliable and useless. With the aim to avoid, or alleviate the shear locking issue, various of novel numerical techniques have been developed with varying degree of success.

The reduced and selective integration scheme proposed by Hughes et al. was used to overcome the shear locking issue [10]. In Hughes' work, the strain energy was split into two parts: the shear part and bending part, different strain energy parts are obtained from different integration schemes. It is found that the reduced and selective integration scheme is effective to overcome the shear locking issue. Unfortunately, these integration often lead to an instability and exhibit zero energy modes. Bathe and his colleagues proposed the “mixed interpolation of tensorical components” (MITC) to handle shear locking issue [11,12]. In MITC technique, the strains and displacements are interpolated separately and the separate interpolations are connected at “tying points”. In addition, the choice of these interpolations should obey the ellipticity and consistency conditions. Based on MITC, the 4-node shell elements (MITC4) was first developed for shell analysis. MacNeal developed the assumed natural strains (ANS) method to tackle the above-mentioned shear locking issue [13]. In the ANS method, the process of computing the element stiffness matrices is based on an assumed strain field rather than an assumed displacement field. Recently, a novel discrete shear gap technique (DSG), which is a little similar to the ANS method, is proposed by Bletzinger et al. [14] to deal with the shear locking issue for plates and shells. In the DSG method, only nodal displacements are used to form the relevant element stiffness matrices. Hence it is very simple and easy to implement. It is found that the DSG method removes the shear locking issue successfully and works fairly well for both rectangular and triangular elements.

Another challenge in the standard FEM analysis for shells is that these standard FEM models always behave “overly-stiff” and provide low degree of accuracy solutions. Recently, with the aim to properly soften the “overly-stiff” FEM models and obtain more accurate numerical solutions, Liu and his colleagues have proposed the novel weakened weakform (or W^2) based on G space theory [15–18], which is in contrast to the standard weakform for standard FEM models, to solve the partial differential equations in solid mechanics problems. Using the weakened weakform and the gradient smoothing technique (GST), Liu et al. have developed a series of smoothed finite element methods (S-FEMs) in recent years [19–37]. In contrast to the point interpolation method (PIM) [38–41] and smoothed particle hydrodynamics (SPH) [42–44] method, which are typical meshfree methods, the S-FEMs are derived by incorporating the gradient smoothing techniques from the meshless techniques into the classical FEM. Therefore, the S-FEMs not only have good features from the FEM but also possess some particular properties from the meshfree methods.

Compared to the original FEM, the S-FEMs possess many excellent properties. Due to weakened weakform and the GST, the system stiffness from S-FEMs models have been properly softened and is closer to the exact one. Therefore, the S-FEMs models could usually provide better solutions compared to the original FEM. The S-FEMs were initially employed to handle linear elastic solid mechanics problems. Owing to the good and attractive properties, the S-FEMs have been applied to many other fields, such as fluid–structure interaction problems [45], acoustics [46–54], functionally graded plates [55], geometrical nonlinear problems [56] and heat transfer problems [57,58].

In the S-FEM family, the node-based smoothed FEM (NS-FEM) is derived by incorporating the node-based gradient smoothing technique (N-GST) into the standard FEM [59,60]. It has been proved that the NS-FEM usually behaves “overly-soft”, which is exactly opposed to the “overly-stiff” FEM, and can provide upper bound solutions to solid mechanics [59]. However, due to the “overly-soft” behavior, the NS-FEM suffers from the temporal instability property [61]. Therefore, it cannot be used directly to handle nonlinear problems and dynamic problems. With the aim to overcome this, a novel hybrid smoothed FEM (HS-FEM) has been developed by combining the NS-FEM with the standard FEM with the help of a scale factor α [62]. In some published literatures, it is also called as alpha finite element method (α -FEM) [63–66]. It has been shown that the HS-FEM (or α -FEM) can provide better solutions for mechanics problems than either NS-FEM or standard FEM. Recently, Nguyen-Thoi et al. have developed the coupled NS-FEM and the DSG [14,34,67,68] with triangular elements (NS-DSG3) to analyze plate structures. Likewise, owing to the “overly-soft” NS-FEM, the NS-DSG3 also is unable to handle dynamic problems of plates and some special stabilization techniques are needed. Based on the HS-FEM ideas, the present work makes attempts to build the relationship between the DSG3 and NS-DSG3 for shells so as to synergize the individual advantages of the two methods. The related formulation is named as hybrid smoothed discrete shear gap (HS-DSG3) in this work. In the HS-DSG3 model, the N-GST is used to obtain the node-based smoothed strain field, then a new strain field, which contains both the strain components from standard DSG3 and the strain components from NS-DSG3, is reconstructed with the help of a scale factor $\alpha \in [0, 1]$. The system stiffness of the new model lies exactly between the “overly-soft” NS-DSG3 model and the “overly-stiff” DSG3 model, so it is relatively reasonable to describe the real strain field for shells. Therefore, the present HS-DSG3 is very promising to improve the degree of the solution accuracy for shell analysis.

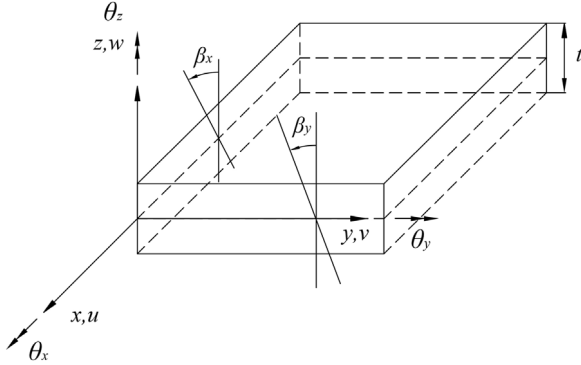


Fig. 1. The typical shell element with positive directions of displacements u , v , w and rotations θ_x , θ_y , θ_z .

The organization of present work is as follows: the next section includes the standard Galerkin weakform for shells. Section 3 briefly describes the general Reissner–Mindlin plate/shell element formulation. The formulation of hybrid smoothed discrete shear gap method for shells is presented in Section 4 in detail. The formulation of the geometrical nonlinear problems is presented in Section 5. Section 6 includes several typical numerical examples. The final conclusions are presented in Section 7.

2. The standard weakform for shell structures

In general, the shell structures must possess stretching and bending deformation. Therefore the shell element could be considered approximately as the superposition of the membrane element and the plate bending element. A typical shell element subjected to both bending loading and membrane loading is shown in Fig. 1, the reference plane is the middle surface of the shell. For Reissner–Mindlin plate/shell element, the six independent field variables is expressed by

$$\mathbf{u} = [u \quad v \quad w \quad \theta_x \quad \theta_y \quad \theta_z]^T \quad (1)$$

where u , v and w represent the displacement variables in the x , y and z directions, θ_x , θ_y and θ_z denote the rotations with respect to x , y and z axes.

During the deformation, all the normals to the neutral plane should be straight based on the Reissner–Mindlin assumption. However, they are not required to be perpendicular to neutral plane after the deformation. Then the curvature κ and transverse shear strain γ can be expressed by

$$\kappa = \begin{bmatrix} \frac{\partial \theta_y}{\partial x} \\ -\frac{\partial \theta_x}{\partial x} \\ \frac{\partial \theta_y}{\partial y} - \frac{\partial \theta_x}{\partial x} \end{bmatrix}, \quad \gamma = \begin{bmatrix} \frac{\partial w}{\partial x} + \theta_y \\ \frac{\partial w}{\partial y} - \theta_x \end{bmatrix}. \quad (2)$$

For linear analysis, the membrane strain components $\boldsymbol{\epsilon}_m$ is given by:

$$\boldsymbol{\epsilon}_m = \boldsymbol{\epsilon}_m^l = \begin{bmatrix} \frac{\partial u}{\partial x} \\ \frac{\partial v}{\partial y} \\ \frac{\partial u}{\partial y} + \frac{\partial v}{\partial x} \end{bmatrix}. \quad (3)$$

For nonlinear analysis,

$$\boldsymbol{\epsilon}_m = \boldsymbol{\epsilon}_m^l + \boldsymbol{\epsilon}_m^{nl} = \begin{bmatrix} \frac{\partial u}{\partial x} \\ \frac{\partial v}{\partial y} \\ \frac{\partial u}{\partial y} + \frac{\partial v}{\partial x} \end{bmatrix} + \begin{bmatrix} \frac{1}{2} \left(\frac{\partial w}{\partial x} \right)^2 \\ \frac{1}{2} \left(\frac{\partial w}{\partial y} \right)^2 \\ \frac{\partial w}{\partial x} \frac{\partial w}{\partial y} \end{bmatrix} \quad (4)$$

in which $\boldsymbol{\epsilon}_m^l$ and $\boldsymbol{\epsilon}_m^{nl}$ represent the linear part and nonlinear part, respectively.

Then the constitutive relationship is given by

$$\hat{\sigma} = \hat{\mathbf{D}}\hat{\boldsymbol{\epsilon}} \quad (5)$$

where

$$\hat{\boldsymbol{\sigma}} = \begin{bmatrix} \hat{\mathbf{N}} \\ \hat{\mathbf{M}} \\ \hat{\mathbf{Q}} \end{bmatrix}, \quad \hat{\mathbf{D}} = \begin{bmatrix} \mathbf{D}_m & \mathbf{0} & \mathbf{0} \\ \mathbf{0} & \mathbf{D}_b & \mathbf{0} \\ \mathbf{0} & \mathbf{0} & \mathbf{D}_s \end{bmatrix}, \quad \hat{\boldsymbol{\epsilon}} = \begin{bmatrix} \boldsymbol{\epsilon}_m \\ \boldsymbol{\epsilon}_b \\ \boldsymbol{\epsilon}_s \end{bmatrix} \quad (6)$$

where $\hat{\mathbf{N}} = [N_x \ N_y \ N_{xy}]^T$ represents the membrane force vector, $\hat{\mathbf{Q}} = [Q_x \ Q_y]^T$ represents the transverse shear force vector, $\hat{\mathbf{M}} = [M_x \ M_y \ M_{xy}]^T$ represents the bending moment vector, \mathbf{D}_m , \mathbf{D}_s and \mathbf{D}_b are the related stiffness constitutive coefficients.

For the static analysis, the standard Galerkin weakform can be obtained by using the principle of virtual work.

$$\int_{\Omega} (\delta \boldsymbol{\epsilon}_m)^T \mathbf{D}_m \boldsymbol{\epsilon}_m d\Omega + \int_{\Omega} \delta \kappa^T \mathbf{D}_b \kappa d\Omega + \int_{\Omega} \delta \gamma^T \mathbf{D}_s \gamma d\Omega - \int_{\Omega} \delta \mathbf{u}^T \mathbf{b} d\Omega - \int_{\Gamma} \delta \mathbf{u}^T \mathbf{t} d\Gamma = 0 \quad (7)$$

where δ denotes the variational operator, \mathbf{b} and \mathbf{t} represent the body force vector and the surface traction vector, respectively.

Assuming the materials of the plates or shells are isotropic and homogeneous, we have

$$\mathbf{D}_m = \frac{Et}{(1-v^2)} \begin{bmatrix} 1 & v & 0 \\ v & 1 & 0 \\ 0 & 0 & 1-v/2 \end{bmatrix} \quad (8)$$

$$\mathbf{D}_b = \frac{Et^3}{12(1-v^2)} \begin{bmatrix} 1 & v & 0 \\ v & 1 & 0 \\ 0 & 0 & 1-v/2 \end{bmatrix} \quad (9)$$

$$\mathbf{D}_s = \kappa t G \begin{bmatrix} 1 & 0 \\ 0 & 1 \end{bmatrix} \quad (10)$$

where $\kappa = 5/6$ denotes the shear correction factor, E and G represent the Young's modulus and the shear modulus, t and v represent the thickness and the Poisson's ratio.

The standard weakform for dynamic analysis is given by

$$\int_{\Omega} (\delta \boldsymbol{\epsilon}_m)^T \mathbf{D}_m \boldsymbol{\epsilon}_m d\Omega + \int_{\Omega} \delta \kappa^T \mathbf{D}_b \kappa d\Omega + \int_{\Omega} \delta \gamma^T \mathbf{D}_s \gamma d\Omega + \int_{\Omega} \delta \mathbf{u}^T \mathbf{m} \ddot{\mathbf{u}} d\Omega + \int_{\Omega} \delta \mathbf{u}^T \mathbf{c} \dot{\mathbf{u}} d\Omega - \int_{\Omega} \delta \mathbf{u}^T \mathbf{b} d\Omega - \int_{\Gamma} \delta \mathbf{u}^T \mathbf{t} d\Gamma = 0 \quad (11)$$

where \mathbf{c} and \mathbf{m} represent the damping matrix and mass matrix, respectively.

In the free vibration analysis case, if there is no damping effects, Eq. (11) can be rewritten as

$$\int_{\Omega} (\delta \boldsymbol{\epsilon}^m)^T \mathbf{D}_m \boldsymbol{\epsilon}^m d\Omega + \int_{\Omega} \delta \kappa^T \mathbf{D}_b \kappa d\Omega + \int_{\Omega} \delta \gamma^T \mathbf{D}_s \gamma d\Omega + \int_{\Omega} \delta \mathbf{u}^T \mathbf{m} \ddot{\mathbf{u}} d\Omega = 0 \quad (12)$$

where the mass matrix \mathbf{m} is defined as

$$\mathbf{m} = \text{diag} [\rho t \ \rho t \ \rho t \ \rho t^3/12 \ \rho t^3/12 \ 0] \quad (13)$$

where ρ is the density of the material.

3. The general Reissner–Mindlin plate/shell element formulation

Assuming that the bounded problem domain has been partitioned into N_e elements, such that $\Omega = \cup_{e=1}^{N_e} \Omega_e$ and $\Omega_i \cap \Omega_j = \emptyset, i \neq j$, then the finite element solutions for the shell structures can be expressed by

$$\mathbf{u} = \sum_{I=1}^{N_n} \mathbf{N}_I \mathbf{u}_I \quad (14)$$

where $\mathbf{u}_I = [u_I \ v_I \ w_I \ \theta_{xI} \ \theta_{yI} \ \theta_{zI}]^T$ is the generalized nodal displacement in natural coordinate system for node I , N_n denotes the number of nodes. \mathbf{N}_I denotes a diagonal matrix which containing the FEM shape functions.

$$\mathbf{N}_I = \text{diag} [N_I(\mathbf{x}) \ N_I(\mathbf{x}) \ N_I(\mathbf{x}) \ N_I(\mathbf{x}) \ N_I(\mathbf{x}) \ N_I(\mathbf{x})]. \quad (15)$$

Then the above-mentioned strain components can be given by

$$\begin{aligned}\boldsymbol{\varepsilon}_m^l &= \sum_{l=1}^{N_n} \mathbf{B}_{ml}^l \mathbf{u}_l \\ \boldsymbol{\varepsilon}_m^{nl} &= \sum_{l=1}^{N_n} \frac{1}{2} \mathbf{B}_{ml}^{nl} \mathbf{u}_l \\ \boldsymbol{\kappa} &= \sum_{l=1}^{N_n} \mathbf{B}_{bl} \mathbf{u}_l \\ \boldsymbol{\gamma} &= \sum_{l=1}^{N_n} \mathbf{B}_{sl} \mathbf{u}_l\end{aligned}\tag{16}$$

where

$$\mathbf{B}_{ml} = \begin{bmatrix} \partial N_l / \partial x & 0 & 0 & 0 & 0 & 0 \\ 0 & \partial N_l / \partial y & 0 & 0 & 0 & 0 \\ \partial N_l / \partial y & \partial N_l / \partial x & 0 & 0 & 0 & 0 \end{bmatrix}\tag{17}$$

$$\mathbf{B}_{bl} = \begin{bmatrix} 0 & 0 & 0 & \partial N_l / \partial x & 0 \\ 0 & 0 & -\partial N_l / \partial y & 0 & 0 \\ 0 & 0 & -\partial N_l / \partial x & \partial N_l / \partial y & 0 \end{bmatrix}\tag{18}$$

$$\mathbf{B}_{sl} = \begin{bmatrix} 0 & 0 & \partial N_l / \partial x & 0 & N_l & 0 \\ 0 & 0 & \partial N_l / \partial y & -N_l & 0 & 0 \end{bmatrix}\tag{19}$$

$$\mathbf{B}_{ml}^{nl} = \mathbf{A}_l \mathbf{G}_{kl}\tag{20}$$

in which

$$\mathbf{A}_l = \begin{bmatrix} \frac{\partial N_l}{\partial x} w_l & 0 & \frac{\partial N_l}{\partial y} w_l \\ 0 & \frac{\partial N_l}{\partial y} w_l & \frac{\partial N_l}{\partial x} w_l \end{bmatrix}^T\tag{21}$$

$$\mathbf{G}_l = \begin{bmatrix} 0 & 0 & \partial N_l / \partial x & 0 & 0 & 0 \\ 0 & 0 & \partial N_l / \partial y & 0 & 0 & 0 \end{bmatrix}.\tag{22}$$

For static analysis, the system equation could be formulated from the standard FEM formulation

$$\mathbf{Ku} = \mathbf{f}\tag{23}$$

where \mathbf{K} represents the global stiffness matrix.

$$\mathbf{K} = \sum_{i=1}^{N_e} \int_{\Omega_i^e} (\mathbf{B}_i)^T \mathbf{D} \mathbf{B}_i d\Omega = \sum_{i=1}^{N_e} (\mathbf{K}_i^l + \mathbf{K}_i^{nl})\tag{24}$$

where Ω_i^e denotes the area of the i th element, N_e denotes the number of elements, $\mathbf{D} = \text{diag} [\mathbf{D}_m \quad \mathbf{D}_b \quad \mathbf{D}_s]$ is the related stiffness constitutive coefficients; \mathbf{B}_i is the strain matrix; \mathbf{K}_i^l and \mathbf{K}_i^{nl} are the linear and nonlinear term in the element stiffness matrix.

$$\mathbf{B}_i = \mathbf{B}_i^l + \mathbf{B}_i^{nl} = \begin{bmatrix} \mathbf{B}_{mi}^l \\ \mathbf{B}_{bi}^l \\ \mathbf{B}_{si}^l \end{bmatrix} + \begin{bmatrix} \mathbf{B}_{mi}^{nl} \\ \mathbf{0} \\ \mathbf{0} \end{bmatrix}\tag{25}$$

$$\mathbf{K}_i^l = \mathbf{K}_{mi}^l + \mathbf{K}_{bi}^l + \mathbf{K}_{si}^l = \left[(\mathbf{B}_{mi}^l)^T \mathbf{D}_m \mathbf{B}_{mi}^l + (\mathbf{B}_{bi}^l)^T \mathbf{D}_b \mathbf{B}_{bi}^l + (\mathbf{B}_{si}^l)^T \mathbf{D}_s \mathbf{B}_{si}^l \right] A_i\tag{26}$$

$$\mathbf{K}_i^{nl} = \left[\frac{1}{2} (\mathbf{B}_i^l)^T \mathbf{D} \mathbf{B}_i^{nl} + (\mathbf{B}_i^{nl})^T \mathbf{D} \mathbf{B}_i^l + \frac{1}{2} (\mathbf{B}_i^{nl})^T \mathbf{D} \mathbf{B}_i^{nl} \right] A_i.\tag{27}$$

The global excitation force vector is given by

$$f = \int_{\Omega} \mathbf{N}^T \mathbf{b} d\Omega + \mathbf{f}_b = \sum_{i=1}^{N_e} \int_{\Omega_i^e} \mathbf{N}^T \mathbf{b} d\Omega + \mathbf{f}_b\tag{28}$$

in which \mathbf{b} and \mathbf{f}_b represent the body loading and the prescribed boundary loading, respectively.

For free vibration analysis case, the force vector is not considered and we have

$$(\mathbf{K} - \omega^2 \mathbf{M}) \mathbf{d} = 0 \quad (29)$$

where ω is the angular frequency.

4. The formulation of hybrid smoothed DSG technique (HS-DSG) for shell structures

4.1. The discrete shear gap technique (DSG)

The shear locking issue always arises when the thickness is very small for Reissner–Mindlin plate and shell structures. The shear locking results in an additional, artificial stiffness to the system and leads to inaccurate numerical solutions. What is more, this locking effects will be even more severe with the decrease of the thickness. With the aim to overcome this problem, a novel discrete shear gap (DSG) technique has been proposed by Bletzinger et al. [14] for plates and shells with very small thickness. It is found that the DSG can remove the shear locking issue successfully and possesses several superior properties. The detailed formulation of DSG technique for three-node triangular element (DSG3) will be presented in the following section.

In the DSG3 model, the following simple linear shape functions (see Fig. 2) is used

$$N_1 = 1 - \xi - \eta, \quad N_2 = \xi, \quad N_3 = \eta. \quad (30)$$

Then the linear membrane strains $\boldsymbol{\epsilon}_m^l$ and curvature κ can be obtained by

$$\boldsymbol{\epsilon}_m^l = \begin{bmatrix} \mathbf{B}_{m1}^l & \mathbf{B}_{m2}^l & \mathbf{B}_{m3}^l \\ \hline \mathbf{B}_m^l & & \end{bmatrix} \mathbf{u}_l = \mathbf{B}_m^l \mathbf{u}_l \quad (31)$$

$$\kappa = \begin{bmatrix} \mathbf{B}_{b1} & \mathbf{B}_{b2} & \mathbf{B}_{b3} \\ \hline \mathbf{B}_b & & \end{bmatrix} \mathbf{u}_l = \mathbf{B}_b \mathbf{u}_l \quad (32)$$

where \mathbf{B}_m^l and \mathbf{B}_b are the strain matrices. It is clear that they are constant for each element because the shape functions used are linear.

$$\mathbf{B}_{m1}^l = \frac{1}{2A_e} \begin{bmatrix} b-d & 0 & 0 & 0 & 0 & 0 \\ 0 & c-a & 0 & 0 & 0 & 0 \\ c-a & b-d & 0 & 0 & 0 & 0 \end{bmatrix} \quad (33)$$

$$\mathbf{B}_{m2}^l = \frac{1}{2A_e} \begin{bmatrix} d & 0 & 0 & 0 & 0 & 0 \\ 0 & -c & 0 & 0 & 0 & 0 \\ -c & d & 0 & 0 & 0 & 0 \end{bmatrix} \quad (34)$$

$$\mathbf{B}_{m3}^l = \frac{1}{2A_e} \begin{bmatrix} -b & 0 & 0 & 0 & 0 & 0 \\ 0 & a & 0 & 0 & 0 & 0 \\ a & -b & 0 & 0 & 0 & 0 \end{bmatrix} \quad (35)$$

$$\mathbf{B}_{b1} = \frac{1}{2A_e} \begin{bmatrix} 0 & 0 & 0 & 0 & b-d & 0 \\ 0 & 0 & 0 & a-c & 0 & 0 \\ 0 & 0 & 0 & d-b & c-a & 0 \end{bmatrix} \quad (36)$$

$$\mathbf{B}_{b2} = \frac{1}{2A_e} \begin{bmatrix} 0 & 0 & 0 & 0 & d & 0 \\ 0 & 0 & 0 & c & 0 & 0 \\ 0 & 0 & 0 & -d & -c & 0 \end{bmatrix} \quad (37)$$

$$\mathbf{B}_{b3} = \frac{1}{2A_e} \begin{bmatrix} 0 & 0 & 0 & 0 & -b & 0 \\ 0 & 0 & 0 & -a & 0 & 0 \\ 0 & 0 & 0 & b & a & 0 \end{bmatrix} \quad (38)$$

with $a = x_2 - x_1$, $b = y_2 - y_1$, $c = x_3 - x_1$, $d = y_3 - y_1$ (see Fig. 2) and A_e denotes the area of each element.

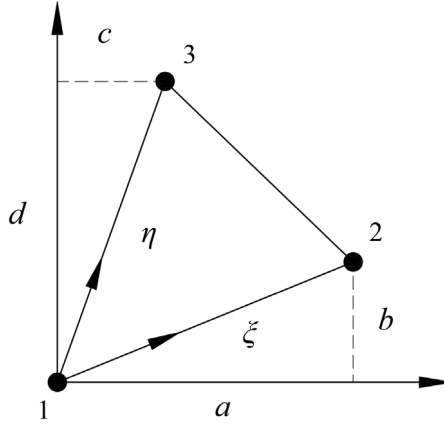


Fig. 2. The three-node triangular element in natural coordinate system.

In the DSG3 formulation, the shear strain components in each triangular element is given by

$$\gamma_{xz} = \sum_{l=1}^3 \frac{\partial N_l(\mathbf{x})}{\partial x} \Delta w_{xl} + \sum_{l=1}^3 \frac{\partial N_l(\mathbf{x})}{\partial x} \Delta w_{yl} \quad (39)$$

$$\gamma_{yz} = \sum_{l=1}^3 \frac{\partial N_l(\mathbf{x})}{\partial y} \Delta w_{xl} + \sum_{l=1}^3 \frac{\partial N_l(\mathbf{x})}{\partial y} \Delta w_{yl} \quad (40)$$

in which w_{xl} and w_{yl} denote the corresponding discrete shear gaps for each node in the triangular element.

$$\Delta w_{x1} = \Delta w_{x3} = \Delta w_{y1} = \Delta w_{y2} = 0 \quad (41)$$

$$\Delta w_{x2} = (w_2 - w_1) - \frac{1}{2}b(\theta_{x1} + \theta_{x2}) + \frac{1}{2}a(\theta_{y1} + \theta_{y2}) \quad (42)$$

$$\Delta w_{y3} = (w_3 - w_1) - \frac{1}{2}d(\theta_{x1} + \theta_{x3}) + \frac{1}{2}c(\theta_{y1} + \theta_{y3}). \quad (43)$$

Then the shear strain components can be calculated by

$$\gamma = \left[\underbrace{\mathbf{B}_{s1} \quad \mathbf{B}_{s2} \quad \mathbf{B}_{s3}}_{\mathbf{B}_s} \right] \mathbf{u}_I = \mathbf{B}_s \mathbf{u}_I \quad (44)$$

in which the shear strain matrix \mathbf{B}_s is given by

$$\mathbf{B}_{s1} = \frac{1}{2A_e} \begin{bmatrix} 0 & 0 & b-d & 0 & -A_e & 0 \\ 0 & 0 & c-a & -A_e & 0 & 0 \end{bmatrix} \quad (45)$$

$$\mathbf{B}_{s2} = \frac{1}{2A_e} \begin{bmatrix} 0 & 0 & d & -\frac{bd}{2} & \frac{ad}{2} & 0 \\ 0 & 0 & -c & \frac{bc}{2} & -\frac{ac}{2} & 0 \end{bmatrix} \quad (46)$$

$$\mathbf{B}_{s3} = \frac{1}{2A_e} \begin{bmatrix} 0 & 0 & -b & \frac{bd}{2} & -\frac{bc}{2} & 0 \\ 0 & 0 & a & -\frac{ad}{2} & \frac{ac}{2} & 0 \end{bmatrix}. \quad (47)$$

With the aim to stabilize the shear force oscillations and enhance the performance of the DSG3 method for shells structures, a stabilization term is added to the shear stiffness constitutive coefficient [34], then the matrix \mathbf{D}_s in the original

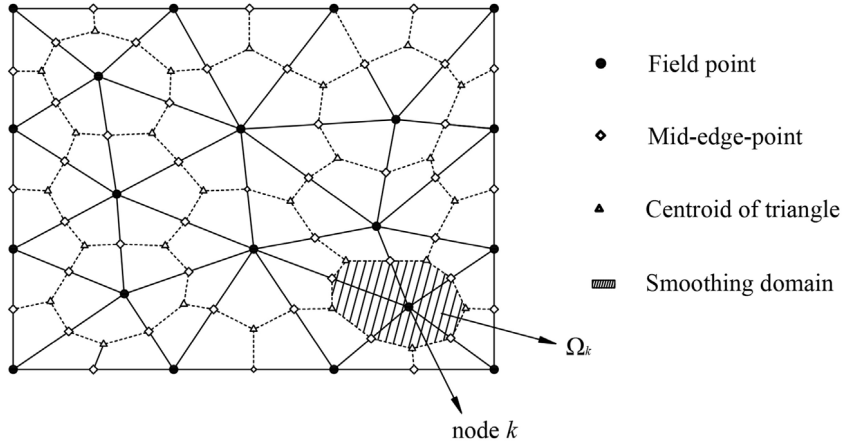


Fig. 3. The node-based smoothing domain for two-dimensional problems.

DSG3 formulation will be replaced by $\hat{\mathbf{D}}_s$

$$\hat{\mathbf{D}}_s = \frac{G\kappa t^3}{t^2 + \beta h_e^2} \begin{bmatrix} 1 & 0 \\ 0 & 1 \end{bmatrix} \quad (48)$$

in which β is a positive constant and h_e denotes the longest edges in the triangular element [69].

4.2. The treatment of the drilling degree of freedom

In the previous formulation, each node in the shell element consists of three rotation degrees of freedom (DOFs) and three displacement DOFs. Actually, the third rotation degree “ θ_{zi} ”, which is the so-called drilling degree of freedom, is not necessary to construct the theoretical foundation. However, the inclusion of the third rotation degree has obvious advantages in programming and computation because both rotations and displacements at nodes can be treated in a simple manner using the coordinate transformation procedure. Unfortunately, when this six DOFs type shell element is used to solve shell segments or folded plate structures, a difficulty always arises if all the elements sharing the same node are co-planar. The difficulty results from the zero stiffness in the θ_{zi} direction and this always causes the singular behavior. In order to avoid the presence of this singular behavior, an extra arbitrary coefficient $k_{\theta_{zi}}$ is inserted at the related DOF θ_{zi} in this work, then the related equation can be expressed as

$$k_{\theta_{zi}} \theta_{zi} = 0. \quad (49)$$

Here the value of the arbitrary stiffness coefficient $k_{\theta_{zi}}$ is chosen to be 10^{-3} of times the maximum diagonal value of the element stiffness matrix [70]. Then the stiffness matrix for node i can be obtained as

$$\mathbf{k}_i = \begin{bmatrix} [\mathbf{k}_p]_{2 \times 2} & \mathbf{0}_{2 \times 3} & 0 \\ \mathbf{0}_{3 \times 2} & [\mathbf{k}_b]_{3 \times 3} & 0 \\ 0 & 0 & 10^{-3} \max(k_{i,i}) \end{bmatrix} \quad (50)$$

in which \mathbf{k}_p and \mathbf{k}_b is the related stiffness matrix corresponding to in-plane and bending actions, respectively.

4.3. The node-based gradient smoothing technique (N-GST)

In this section, the detailed formulation of the N-GST, which will be used to smooth the original strain field, will be presented. To perform the node-based gradient smoothing operation. We should firstly obtain the corresponding node-based smoothing domains. The involved two dimensional space is partitioned into triangular mesh and the whole problem domain consists of N_e elements and N_n nodes (see Fig. 3). Based on this background mesh, the required smoothing domain is formed by linking the middle point of each edge and the centers of the surrounding triangular elements in sequence. As a result, the original problems domain Ω is then discretized into N_s node-based smoothing domains such that $\Omega = \bigcup_{s=1}^{N_s} \Omega_s$ and $\Omega_i \cap \Omega_j = \emptyset, i \neq j$, each smoothing domain is attached to the designated node. In addition, we should note that the number of the obtained smoothing domains is equal to the number of nodes, namely $N_n = N_s$. After obtaining these required node-based smoothing domains, the N-GST can be performed and a new smoothed strain field can be obtained. In fact, the

corresponding numerical integration here is implemented over the smoothing domains rather than the original triangular elements. Therefore, the smoothed strain components for the smoothing domain Ω_k^s associated with node k are given by

$$\begin{aligned}\bar{\boldsymbol{\epsilon}}_m^l &= \int_{\Omega_k^s} \boldsymbol{\epsilon}_m^l(\mathbf{x}_k) \phi_k(\mathbf{x}) d\Omega \\ \bar{\boldsymbol{\epsilon}}_m^{nl} &= \int_{\Omega_k^s} \boldsymbol{\epsilon}_m^{nl}(\mathbf{x}) \phi_k(\mathbf{x}) d\Omega \\ \bar{\boldsymbol{\epsilon}}_b &= \int_{\Omega_k^s} \boldsymbol{\epsilon}_b(\mathbf{x}_k) \phi_k(\mathbf{x}) d\Omega \\ \bar{\boldsymbol{\epsilon}}_s &= \int_{\Omega_k^s} \boldsymbol{\epsilon}_s(\mathbf{x}_k) \phi_k(\mathbf{x}) d\Omega\end{aligned}\quad (51)$$

where $\phi_k(\mathbf{x})$ is the smoothing function defined by

$$\phi_k(\mathbf{x}) = \begin{cases} 1/A_k^s & \mathbf{x} \in \Omega_k^s \\ 0 & \mathbf{x} \notin \Omega_k^s \end{cases} \quad (52)$$

where A_k represents the area of the smoothing domain Ω_k^s .

From the above formulation, we have

$$\begin{aligned}\bar{\boldsymbol{\epsilon}}_m^l &= \frac{1}{A_k} \int_{\Omega_k^s} \boldsymbol{\epsilon}_m^l(\mathbf{x}_k) d\Omega = \sum_{l=1}^{N_n^k} \bar{\mathbf{B}}_{ml}^l(\mathbf{x}_k) \mathbf{u}_l \\ \bar{\boldsymbol{\epsilon}}_m^{nl} &= \frac{1}{A_k} \int_{\Omega_k^s} \boldsymbol{\epsilon}_m^{nl}(\mathbf{x}_k) d\Omega = \sum_{l=1}^{N_n^k} \bar{\mathbf{B}}_{ml}^{nl}(\mathbf{x}_k) \mathbf{u}_l \\ \bar{\boldsymbol{\epsilon}}_b &= \frac{1}{A_k} \int_{\Omega_k^s} \boldsymbol{\epsilon}_b(\mathbf{x}_k) d\Omega = \sum_{l=1}^{N_n^k} \bar{\mathbf{B}}_{bl}^l(\mathbf{x}_k) \mathbf{u}_l \\ \bar{\boldsymbol{\epsilon}}_s &= \frac{1}{A_k} \int_{\Omega_k^s} \boldsymbol{\epsilon}_s(\mathbf{x}_k) d\Omega = \sum_{l=1}^{N_n^k} \bar{\mathbf{B}}_{sl}^l(\mathbf{x}_k) \mathbf{u}_l\end{aligned}\quad (53)$$

where N_n^k denotes the number of triangular elements. $\bar{\mathbf{B}}_{ml}$, $\bar{\mathbf{B}}_{bl}$ and $\bar{\mathbf{B}}_{sl}$ represent the smoothed strain matrices and are expressed by

$$\begin{aligned}\bar{\mathbf{B}}_{ml}^l(\mathbf{x}_k) &= \frac{1}{A_k^s} \sum_{e=1}^{N_e^k} \frac{1}{3} A_k^e \mathbf{B}_{ml}^l(\mathbf{x}_k) \\ \bar{\mathbf{B}}_{ml}^{nl}(\mathbf{x}_k) &= \frac{1}{A_k^s} \sum_{e=1}^{N_e^k} \frac{1}{3} A_k^e \mathbf{B}_{ml}^{nl}(\mathbf{x}_k) \\ \bar{\mathbf{B}}_{bl}^l(\mathbf{x}_k) &= \frac{1}{A_k^s} \sum_{e=1}^{N_e^k} \frac{1}{3} A_k^e \mathbf{B}_{bl}^l(\mathbf{x}_k) \\ \bar{\mathbf{B}}_{sl}^l(\mathbf{x}_k) &= \frac{1}{A_k^s} \sum_{e=1}^{N_e^k} \frac{1}{3} A_k^e \mathbf{B}_{sl}^l(\mathbf{x}_k)\end{aligned}\quad (54)$$

where \mathbf{B}_{ml}^l , \mathbf{B}_{ml}^{nl} , \mathbf{B}_{bl}^l and \mathbf{B}_{sl}^l are the strain matrices for the l th triangular element in the influencing domain. A_k^e denotes the area of this triangular element.

4.4. The hybrid gradient smoothing technique (H-GST)

The N-GST has been presented in the previous sub-section. Using the N-GST, the node-based smoothed FEM (NS-FEM) has been developed for mechanics problems. However, it has been demonstrated that the NS-FEM always behaves “overly-soft” and also suffers from the temporal instability properties. Actually, the NS-FEM cannot be used directly to handle nonlinear problems and dynamic problems unless some stabilization operations are implemented. In order to handle these issues effectively, the hybrid gradient smoothing technique (H-GST) will be presented here. From the previous section, we have known that each triangular element consists of three quadrilateral sub-domains with equal area in the N-GST (or NS-FEM) model. The node-based smoothing domain is exactly a combination of these quadrilateral sub-domains sharing the same

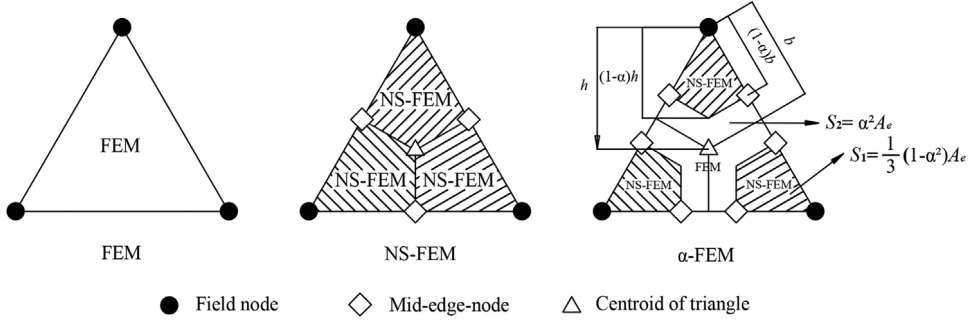


Fig. 4. The process of forming the shrunken smoothing domains for the H-GST model.

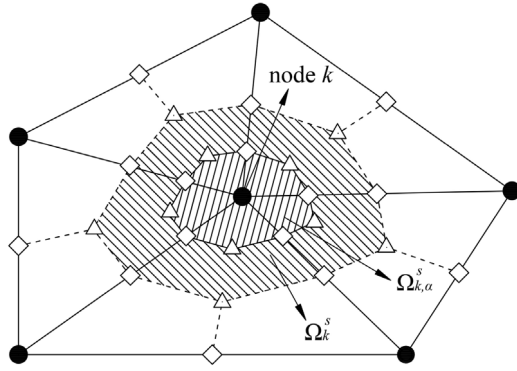


Fig. 5. The shrunken node-based smoothing domain.

node. While in the H-GST model, as shown in Fig. 4, a parameter $\alpha \in [0, 1]$ is used to scale down the three quadrilateral sub-domains. As a result, the original triangular element with an area A_e consists of four parts: three shrunken quadrilateral sub-domains with an equal area of $(1 - \alpha^2) A_e/3$ and the residual Y-shaped sub-domain with an area of $\alpha^2 A_e$.

Then three shrunken quadrilateral sub-domains make contributions to assemble the smoothing element stiffness matrix by using the N-GST (or NS-FEM) scheme and the residual Y-shaped sub-domain makes contribution to assemble the standard element stiffness matrix by using the standard FEM scheme. For convenience of notation, the symbol \mathbf{B} will represent all the above-mentioned strain matrices (\mathbf{B}_m , \mathbf{B}_b , \mathbf{B}_s) \mathbf{D} will represent the corresponding constitutive matrices (\mathbf{D}_m , \mathbf{D}_b , \mathbf{D}_s). Therefore, the global stiffness matrix in H-GST (or HS-FEM) model are given by

$$\bar{\mathbf{K}}^{\text{HS-FEM}} = \sum_{k=1}^{N_n} \bar{\mathbf{K}}_k^{\text{NS-FEM}} + \sum_{i=1}^{N_e} \bar{\mathbf{K}}_i^{\text{FEM}} \quad (55)$$

where

$$\bar{\mathbf{K}}_k^{\text{NS-FEM}} = \int_{\Omega_{k,\alpha}^s} (\bar{\mathbf{B}}^\alpha)^T \mathbf{D} \bar{\mathbf{B}}^\alpha d\Omega \quad (56)$$

$$\bar{\mathbf{K}}_i^{\text{FEM}} = \int_{\Omega_{k,\alpha}^e} \mathbf{B}^T \mathbf{D} \mathbf{B} d\Omega \quad (57)$$

where $\Omega_{k,\alpha}^s$ is the shrunken node-based smoothing domain and bounded by $\Gamma_{k,\alpha}^s$, as shown in Fig. 5. $\Omega_{k,\alpha}^e$ denotes the residual Y-shaped sub-domain.

Actually, for each smoothing domain, the smoothed strain matrix is given by

$$\bar{\mathbf{B}}^\alpha(\mathbf{x}_k) = \frac{1}{A_{k,\alpha}} \sum_{j=1}^{n_k^e} \frac{1}{3} (1 - \alpha^2) A_j^e \mathbf{B}(\mathbf{x}_k) = \frac{1}{A_k^s} \sum_{j=1}^{n_k^e} \frac{1}{3} A_j^e \mathbf{B}(\mathbf{x}_k) = \bar{\mathbf{B}}(\mathbf{x}_k) \quad (58)$$

where $A_{k,\alpha}$ denotes the area of the shrunken smoothing domain $\Omega_{k,\alpha}^s$ and A_k^s denotes the area of the original smoothing domain defined in Fig. 3. n_k^e represents the number of elements in the influencing domain and A_j^e represents the area of the j th triangular element.

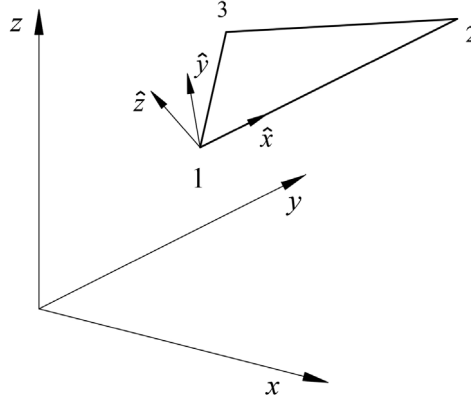


Fig. 6. The local and global coordinates for a triangular element.

From Eq. (58), it is clear that $\bar{\mathbf{B}}^\alpha$ in Eq. (56) could be replaced by $\bar{\mathbf{B}}(\mathbf{x}_k)$ in Eq. (54), then we can have

$$\bar{\mathbf{K}}_k^{\text{NS-FEM}} = (1 - \alpha^2) \left(\int_{\Omega_k^S} \mathbf{B}^T \mathbf{D} \mathbf{B} d\Omega \right). \quad (59)$$

Eqs. (57) and (59) show that the present H-GST (HS-FEM) model is exactly the combination of the standard FEM model and the NS-FEM model. It is reasonable to expect that the present model possesses the individual advantages of the two methods and works well for shell structures.

4.5. The hybrid gradient smoothing technique (H-GST) for shells

Since all the force vectors and element stiffness matrices are based on the local coordinate systems. Therefore, the transformation from a common global coordinate (which is denoted by $x - y - z$) to the local coordinate system (which is denoted by $\hat{x} - \hat{y} - \hat{z}$) is needed to obtain the global stiffness matrix. For each element, the displacements transform between the global coordinate system and the local one is defined by

$$\begin{bmatrix} u_{\hat{x}} \\ v_{\hat{y}} \\ w_{\hat{z}} \\ \theta_{\hat{x}} \\ \theta_{\hat{y}} \\ \theta_{\hat{z}} \end{bmatrix} = \mathbf{T} \begin{bmatrix} u & v & w & \theta_x & \theta_y & \theta_z \end{bmatrix}^T \quad (60)$$

where \mathbf{T} is the transformation matrix and can be expressed as

$$\mathbf{T} = \begin{bmatrix} \Lambda & \mathbf{0} \\ \mathbf{0} & \Lambda \end{bmatrix} \quad (61)$$

in which

$$\Lambda = \begin{bmatrix} \cos(\hat{x}, x) & \cos(\hat{x}, y) & \cos(\hat{x}, z) \\ \cos(\hat{y}, x) & \cos(\hat{y}, y) & \cos(\hat{y}, z) \\ \cos(\hat{z}, x) & \cos(\hat{z}, y) & \cos(\hat{z}, z) \end{bmatrix} = \begin{bmatrix} c_{\hat{x}x} & c_{\hat{x}y} & c_{\hat{x}z} \\ c_{\hat{y}x} & c_{\hat{y}y} & c_{\hat{y}z} \\ c_{\hat{z}x} & c_{\hat{z}y} & c_{\hat{z}z} \end{bmatrix} \quad (62)$$

where $\cos(\hat{x}, x)$ denotes the cosine of the angle between the \hat{x} axis and the x axis, and so on.

The three-node triangular element meshes are used in this work and hence we shall first present the determination of the directions cosine matrix Λ in the triangular element. For a typical triangular element arbitrarily orientated in space, illustrated in Fig. 6, let \hat{x} axis be directed along the side 1-2 of the triangular element. Then this side can be defined by the vector \mathbf{v}_{12} and in the term of global coordinates we have

$$\mathbf{v}_{12} = \begin{bmatrix} x_2 - x_1 \\ y_2 - y_1 \\ z_2 - z_1 \end{bmatrix} = \begin{bmatrix} x_{12} \\ y_{12} \\ z_{12} \end{bmatrix}. \quad (63)$$

Then the cosine of the angle between the \hat{x} and the global system can be easily obtained by

$$\mathbf{v}_{\hat{x}} = \begin{bmatrix} c_{\hat{x}x} \\ c_{\hat{x}y} \\ c_{\hat{x}z} \end{bmatrix} = \frac{1}{\sqrt{x_{12}^2 + y_{12}^2 + z_{12}^2}} \begin{bmatrix} x_{12} \\ y_{12} \\ z_{12} \end{bmatrix}. \quad (64)$$

Once the \hat{x} direction has been determined, then the \hat{z} direction which must be normal to the plane of the element can be established through a “vector” cross-product of two sides of the triangle.

$$\mathbf{v}_{\hat{z}} = \begin{bmatrix} c_{\hat{z}x} \\ c_{\hat{z}y} \\ c_{\hat{z}z} \end{bmatrix} = \frac{\mathbf{V}_{12} \times \mathbf{V}_{13}}{|\mathbf{V}_{12} \times \mathbf{V}_{13}|}. \quad (65)$$

Finally the \hat{y} direction can be determined by the unit vectors $\mathbf{v}_{\hat{x}}$ and $\mathbf{v}_{\hat{z}}$.

$$\mathbf{v}_{\hat{y}} = \begin{bmatrix} c_{\hat{y}x} \\ c_{\hat{y}y} \\ c_{\hat{y}z} \end{bmatrix} = \mathbf{v}_{\hat{z}} \times \mathbf{v}_{\hat{x}} \quad (66)$$

where the sign “ \times ” denotes the cross product of two vectors.

For shell problems, all the strain components in each element are calculated based on the local coordinate system. For the purpose of performing the N-GST over the smoothing domains, a local node coordinate system $\bar{x} - \bar{y} - \bar{z}$, which corresponds to each smoothing domain, is defined in this paper. For convenience of computation, the local coordinate system associated with the first triangular element in the influencing domain is chosen to be this local node coordinate system in practice. Through the transformation rules, the strain components in the each smoothing domain can be defined by

$$\begin{aligned} \bar{\boldsymbol{\epsilon}}_m^l &= \mathbf{R}_{m1} \mathbf{R}_{m2} \hat{\boldsymbol{\epsilon}}_m^l \\ \bar{\boldsymbol{\epsilon}}_m^{nl} &= \mathbf{R}_{m1} \mathbf{R}_{m2} \hat{\boldsymbol{\epsilon}}_m^{nl} \\ \bar{\boldsymbol{\epsilon}}_b &= \mathbf{R}_{b1} \mathbf{R}_{b2} \hat{\boldsymbol{\epsilon}}_b \\ \bar{\boldsymbol{\epsilon}}_s &= \mathbf{R}_{s1} \mathbf{R}_{s2} \hat{\boldsymbol{\epsilon}}_s \end{aligned} \quad (67)$$

in which $\hat{\boldsymbol{\epsilon}}_m^l$, $\hat{\boldsymbol{\epsilon}}_m^{nl}$, $\hat{\boldsymbol{\epsilon}}_b$ and $\hat{\boldsymbol{\epsilon}}_s$ denote strain components in individual element local coordinate system.

$$\mathbf{R}_{m1} = \mathbf{R}_{b1} = \begin{bmatrix} c_{\hat{x}x}^2 & c_{\hat{x}y}^2 & c_{\hat{x}z}^2 & c_{\hat{x}x}c_{\hat{x}y} & c_{\hat{x}y}c_{\hat{x}z} & c_{\hat{x}x}c_{\hat{x}z} \\ c_{\hat{y}x}^2 & c_{\hat{y}y}^2 & c_{\hat{y}z}^2 & c_{\hat{y}x}c_{\hat{y}y} & c_{\hat{y}y}c_{\hat{y}z} & c_{\hat{y}x}c_{\hat{y}z} \\ 2c_{\hat{x}x}c_{\hat{x}y,x} & 2c_{\hat{x}y}c_{\hat{y}y} & 2c_{\hat{x}z}c_{\hat{y}z} & c_{\hat{x}x}c_{\hat{y}y} + c_{\hat{y}x}c_{\hat{x}y} & c_{\hat{x}z}c_{\hat{y}y} + c_{\hat{y}z}c_{\hat{x}y} & c_{\hat{x}x}c_{\hat{y}z} + c_{\hat{y}x}c_{\hat{x}z} \end{bmatrix} \quad (68)$$

$$\mathbf{R}_{s1} = \begin{bmatrix} 2c_{\hat{x}x}c_{\hat{z}x} & 2c_{\hat{x}y}c_{\hat{z}y} & 2c_{\hat{x}z}c_{\hat{z}z} & c_{\hat{x}x}c_{\hat{z}y} + c_{\hat{z}x}c_{\hat{x}y} & c_{\hat{x}z}c_{\hat{z}y} + c_{\hat{z}z}c_{\hat{x}y} & c_{\hat{x}x}c_{\hat{z}z} + c_{\hat{z}x}c_{\hat{x}z} \\ 2c_{\hat{y}x}c_{\hat{z}x} & 2c_{\hat{y}y}c_{\hat{z}y} & 2c_{\hat{y}z}c_{\hat{z}z} & c_{\hat{y}x}c_{\hat{z}y} + c_{\hat{z}x}c_{\hat{y}y} & c_{\hat{y}z}c_{\hat{z}y} + c_{\hat{z}z}c_{\hat{y}y} & c_{\hat{y}x}c_{\hat{z}z} + c_{\hat{z}x}c_{\hat{y}z} \end{bmatrix} \quad (69)$$

$$\mathbf{R}_{m2} = \mathbf{R}_{b2} = \begin{bmatrix} c_{\hat{x}x}^2 & c_{\hat{y}x}^2 & c_{\hat{x}x}c_{\hat{y}x} \\ c_{\hat{x}y}^2 & c_{\hat{y}y}^2 & c_{\hat{x}y}c_{\hat{y}y} \\ c_{\hat{x}z}^2 & c_{\hat{y}z}^2 & c_{\hat{x}z}c_{\hat{y}z} \\ 2c_{\hat{x}x}c_{\hat{x}y} & 2c_{\hat{x}y}c_{\hat{y}y} & c_{\hat{x}x}c_{\hat{y}y} + c_{\hat{x}y}c_{\hat{x}y} \\ 2c_{\hat{x}y}c_{\hat{x}z} & 2c_{\hat{y}y}c_{\hat{y}z} & c_{\hat{x}y}c_{\hat{y}z} + c_{\hat{x}z}c_{\hat{y}y} \\ 2c_{\hat{x}x}c_{\hat{x}z} & 2c_{\hat{x}y}c_{\hat{y}z} & c_{\hat{x}x}c_{\hat{y}z} + c_{\hat{x}z}c_{\hat{y}x} \end{bmatrix} \quad (70)$$

$$\mathbf{R}_{s2} = \begin{bmatrix} c_{\hat{x}x}c_{\hat{z}x} & c_{\hat{y}x}c_{\hat{z}x} \\ c_{\hat{x}y}c_{\hat{z}y} & c_{\hat{y}y}c_{\hat{z}y} \\ c_{\hat{x}z}c_{\hat{z}z} & c_{\hat{y}z}c_{\hat{z}z} \\ c_{\hat{x}x}c_{\hat{z}y} + c_{\hat{x}y}c_{\hat{z}x} & c_{\hat{y}x}c_{\hat{z}y} + c_{\hat{y}y}c_{\hat{z}x} \\ c_{\hat{x}x}c_{\hat{z}z} + c_{\hat{x}z}c_{\hat{z}x} & c_{\hat{y}x}c_{\hat{z}z} + c_{\hat{y}z}c_{\hat{z}x} \\ c_{\hat{x}x}c_{\hat{z}z} + c_{\hat{x}z}c_{\hat{z}x} & c_{\hat{y}x}c_{\hat{z}z} + c_{\hat{y}z}c_{\hat{z}x} \end{bmatrix}. \quad (71)$$

Based on the above formulation, the strain components in the node-based smoothing domain can be written by

$$\begin{aligned} \bar{\boldsymbol{\epsilon}}_m^l &= \mathbf{R}_{m1} \mathbf{R}_{m2} \hat{\mathbf{B}}_m^l \hat{\mathbf{u}} \\ \bar{\boldsymbol{\epsilon}}_m^{nl} &= \mathbf{R}_{m1} \mathbf{R}_{m2} \hat{\mathbf{B}}_m^{nl} \hat{\mathbf{u}} \\ \bar{\boldsymbol{\epsilon}}_b &= \mathbf{R}_{b1} \mathbf{R}_{b2} \hat{\mathbf{B}}_b \hat{\mathbf{u}} \\ \bar{\boldsymbol{\epsilon}}_s &= \mathbf{R}_{s1} \mathbf{R}_{s2} \hat{\mathbf{B}}_s \hat{\mathbf{u}} \end{aligned} \quad (72)$$

in which $\hat{\mathbf{B}}_m^l$, $\hat{\mathbf{B}}_m^{nl}$, $\hat{\mathbf{B}}_b$ and $\hat{\mathbf{B}}_s$ are the strain matrices in element local coordinate system, $\hat{\mathbf{u}}$ is obtained from Eq. (60).

Fig. 7 shows the detailed transformations of coordinate systems. The smoothing domain Ω_k^s corresponding node k consists of several sub-domains. Using the node-based gradient smoothing operation over these sub-domains, the smoothed strain components can be obtained by

$$\begin{aligned}\bar{\boldsymbol{\epsilon}}_m^{k,l} &= \frac{1}{A_k} \sum_{l=1}^{N_n^k} A_{kl} \bar{\boldsymbol{\epsilon}}_m^{kl,l} \\ \bar{\boldsymbol{\epsilon}}_m^{k,nl} &= \frac{1}{A_k} \sum_{l=1}^{N_n^k} A_{kl} \bar{\boldsymbol{\epsilon}}_m^{kl,nl} \\ \bar{\boldsymbol{\epsilon}}_b^k &= \frac{1}{A_k} \sum_{l=1}^{N_n^k} A_{kl} \bar{\boldsymbol{\epsilon}}_b^{kl} \\ \bar{\boldsymbol{\epsilon}}_s^k &= \frac{1}{A_k} \sum_{l=1}^{N_n^k} A_{kl} \bar{\boldsymbol{\epsilon}}_s^{kl}\end{aligned}\tag{73}$$

where $\bar{\boldsymbol{\epsilon}}_m^{kl,l}$, $\bar{\boldsymbol{\epsilon}}_m^{kl,nl}$, $\bar{\boldsymbol{\epsilon}}_b^{kl}$ and $\bar{\boldsymbol{\epsilon}}_s^{kl}$ denote the strain components in the local node coordinate system for the l th triangular element.

Then the strains in terms of global coordinate system can be given by

$$\begin{aligned}\bar{\boldsymbol{\epsilon}}_m^{k,l} &= \frac{1}{A_k} \sum_{l=1}^{N_n^k} A_{kl} \mathbf{R}_{m1}^k \mathbf{R}_{m2}^{kl} \mathbf{B}_m^{kl,l} \mathbf{T}_l \mathbf{u}_l \\ \bar{\boldsymbol{\epsilon}}_m^{k,nl} &= \frac{1}{A_k} \sum_{l=1}^{N_n^k} A_{kl} \mathbf{R}_{m1}^k \mathbf{R}_{m2}^{kl} \mathbf{B}_m^{kl,nl} \mathbf{T}_l \mathbf{u}_l \\ \bar{\boldsymbol{\epsilon}}_b^k &= \frac{1}{A_k} \sum_{l=1}^{N_n^k} A_{kl} \mathbf{R}_{b1}^k \mathbf{R}_{b2}^{kl} \mathbf{B}_b^{kl} \mathbf{T}_l \mathbf{u}_l \\ \bar{\boldsymbol{\epsilon}}_s^k &= \frac{1}{A_k} \sum_{l=1}^{N_n^k} A_{kl} \mathbf{R}_{s1}^k \mathbf{R}_{s2}^{kl} \mathbf{B}_s^{kl} \mathbf{T}_l \mathbf{u}_l\end{aligned}\tag{74}$$

where \mathbf{R}_{m2}^{kl} , \mathbf{R}_{b2}^{kl} and \mathbf{R}_{s2}^{kl} are transformation matrices for l th triangular element, \mathbf{R}_{m1}^k , \mathbf{R}_{b1}^k and \mathbf{R}_{s1}^k are transformation matrices for node k , then the smoothed element stiffness matrix could be obtained from Eq. (54) and the system equation could be solved efficiently.

4.6. Some properties of the HS-DSG3 model for shell structures

As mentioned in the previous section, the proposed HS-DSG3 is derived from DSG3 and NS-DSG3. For the convenience of notation, the strain components (the membrane strain $\boldsymbol{\epsilon}_m$, the curvatures $\boldsymbol{\kappa}$ and the transverse shear strain $\boldsymbol{\gamma}$) are denoted by $\boldsymbol{\epsilon}$ here. Some properties of HS-DSG3 can be drawn as following.

Property 1 (Variational Consistency). In the HS-DSG3 formulation, the usual compatible strain field is used for N_e Y-shaped sub-domain $\Omega_{k,\alpha}^e$ and the smoothed strain field is used for N_n node-based smoothing domain $\Omega_{k,\alpha}^s$. However, the present HS-DSG3 model still possesses the variational consistency property and the detailed process of verifying this will be given here.

Here the modified Hellinger–Reissner variational principle is used and the energy functional can be obtained by

$$\Pi_{HR}(\mathbf{u}, \bar{\boldsymbol{\epsilon}}) = -\frac{1}{2} \int_{\Omega} \bar{\boldsymbol{\epsilon}}^T \mathbf{D} \bar{\boldsymbol{\epsilon}} d\Omega + \int_{\Omega} \bar{\boldsymbol{\epsilon}}^T \mathbf{D} (\nabla \mathbf{u}) d\Omega - \int_{\Omega} \mathbf{u}^T \mathbf{b} d\Omega - \int_{\Gamma} \mathbf{u}^T \mathbf{t} d\Gamma\tag{75}$$

in which \mathbf{D} is the constitutive matrix, \mathbf{u} and $\bar{\boldsymbol{\epsilon}}$ are the assumed displacement and strain variables.

Performing the variation operation, we have

$$\begin{aligned}\delta \Pi_{HR}(\mathbf{u}, \bar{\boldsymbol{\epsilon}}) &= - \int_{\Omega} (\delta \bar{\boldsymbol{\epsilon}})^T \mathbf{D} \bar{\boldsymbol{\epsilon}} d\Omega + \int_{\Omega} (\delta \bar{\boldsymbol{\epsilon}})^T \mathbf{D} (\nabla \mathbf{u}) d\Omega + \int_{\Omega} \bar{\boldsymbol{\epsilon}}^T \mathbf{D} (\nabla \delta \mathbf{u}) d\Omega \\ &\quad - \int_{\Omega} \delta \mathbf{u}^T \mathbf{b} d\Omega - \int_{\Gamma} \delta \mathbf{u}^T \mathbf{t} d\Gamma.\end{aligned}\tag{76}$$

Based on the arbitrary property of variation, the following equation can be obtained by substituting Eqs. (14) and (16) into Eq. (76)

$$\bar{\mathbf{K}} \mathbf{u} = \mathbf{f}\tag{77}$$

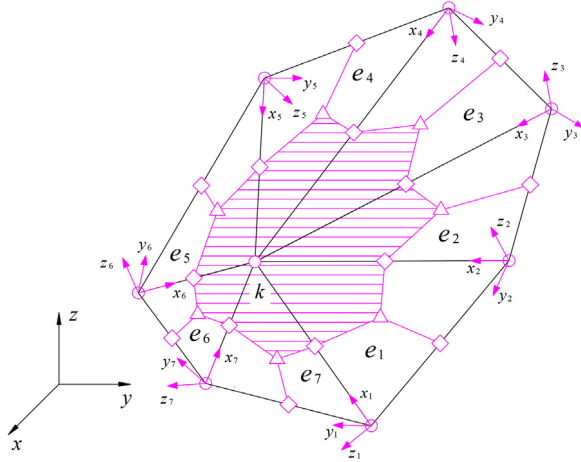


Fig. 7. The N-GST for shell elements.

in which \mathbf{f} represents the force vector and $\bar{\mathbf{K}}$ represents the global stiffness matrix.

$$\bar{\mathbf{K}}_{ij} = - \int_{\Omega_{k,\alpha}^e} \bar{\mathbf{B}}_I^T \mathbf{D} \bar{\mathbf{B}}_j d\Omega + 2 \int_{\Omega_{k,\alpha}^e} \bar{\mathbf{B}}_I^T \mathbf{D} \bar{\mathbf{B}}_j d\Omega - \int_{\Omega_{k,\alpha}^s} \bar{\mathbf{B}}_I^T \mathbf{D} \bar{\mathbf{B}}_j d\Omega + 2 \int_{\Omega_{k,\alpha}^s} \bar{\mathbf{B}}_I^T \mathbf{D} \bar{\mathbf{B}}_j d\Omega \quad (78)$$

$$\mathbf{f} = \int_{\Omega} \mathbf{N}^T(\mathbf{x}) \mathbf{b} d\Omega - \int_{\Gamma} \mathbf{N}^T(\mathbf{x}) \mathbf{t} d\Gamma. \quad (79)$$

Note that $\bar{\mathbf{e}} = \mathbf{e}$ and $\bar{\mathbf{B}}_I = \mathbf{B}_I$ is valid for the Y-shaped domain $\Omega_{k,\alpha}^e$, Eq. (78) can be given by

$$\bar{\mathbf{K}}_{ij} = \int_{\Omega_{k,\alpha}^e} \bar{\mathbf{B}}_I^T \mathbf{D} \bar{\mathbf{B}}_j d\Omega - \int_{\Omega_{k,\alpha}^s} \bar{\mathbf{B}}_I^T \mathbf{D} \bar{\mathbf{B}}_j d\Omega + 2 \int_{\Omega_{k,\alpha}^s} \bar{\mathbf{B}}_I^T \mathbf{D} \bar{\mathbf{B}}_j d\Omega. \quad (80)$$

From Eq. (54), we have

$$\begin{aligned} \int_{\Omega_{k,\alpha}^s} \bar{\mathbf{B}}_I^T \mathbf{D} \bar{\mathbf{B}}_j d\Omega &= \bar{\mathbf{B}}_I^T \mathbf{D} \int_{\Omega_{k,\alpha}^s} \bar{\mathbf{B}}_j d\Omega = \bar{\mathbf{B}}_I^T \mathbf{D} A_{k,\alpha}^s \int_{\Omega_{k,\alpha}^s} \frac{1}{A_{k,\alpha}^s} \bar{\mathbf{B}}_j(\mathbf{x}) d\Omega \\ &= \bar{\mathbf{B}}_I^T \mathbf{D} \bar{\mathbf{B}}_j A_{k,\alpha}^s = \int_{\Omega_{k,\alpha}^s} \bar{\mathbf{B}}_I^T \mathbf{D} \bar{\mathbf{B}}_j d\Omega. \end{aligned} \quad (81)$$

Then Eq. (80) can be rewritten by

$$\bar{\mathbf{K}}_{ij} = \int_{\Omega_{k,\alpha}^e} \bar{\mathbf{B}}_I^T \mathbf{D} \bar{\mathbf{B}}_j d\Omega + \int_{\Omega_{k,\alpha}^s} \bar{\mathbf{B}}_I^T \mathbf{D} \bar{\mathbf{B}}_j d\Omega. \quad (82)$$

In practical computation, Eq. (82) is used to calculate the global stiffness matrix. From Eq. (82), it is obvious that the proposed HS-DSG3 model, which is a combination between DSG3 and NS-DSG3, is variationally consistent.

Property 2 (Stiffer than NS-DSG3). From Eqs. (55) and (59), it is clear that HS-DSG3 becomes NS-DSG3 when $\alpha=0$, while for any $\alpha \in [0, 1]$, the present HS-DSG3 will behave stiffer than NS-DSG3.

Property 3 (Softer than DSG3). When $\alpha = 1$, HS-DSG3 becomes the standard DSG3. From Eq. (55), it is easy to find that: for any $\alpha \in [0, 1]$, the stiffness of the HS-DSG3 is softer than the original DSG3.

Property 4 (Solution Continuity Property). As mentioned in Properties 2 and 3, the stiffness of the HS-DSG3 lies exactly in between the NS-DSG3 and the original DSG3. In addition, from Eq. (55), it is found that the solutions of HS-DSG3 will vary from NS-DSG3 solutions to DSG3 solutions when the value of α varies from 0 to 1. This important property allows us to obtain nearly exact solution by carefully choosing the value of α .

Property 5 (Exact Solution Property). From Properties 2–4, we have known clearly that the strain energy solutions from HS-DSG3 always lie in between those from standard DSG3 and NS-DSG3 when the same mesh is used. In addition, the solution of HS-DSG3 are continuous functions of α . Therefore, it is definite that the exact solution will fall in the range of the HS-DSG3 solution with

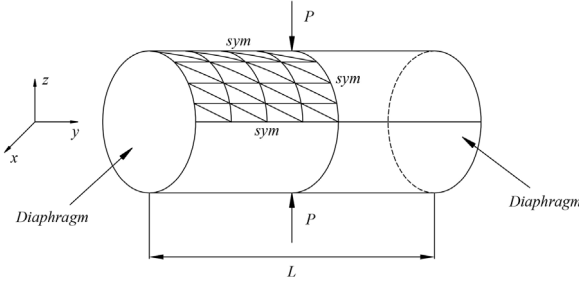


Fig. 8. The pinched cylinder under point load (Poisson's ratio $\nu = 0.3$ and Young's modulus $E = 3 \times 10^7$).

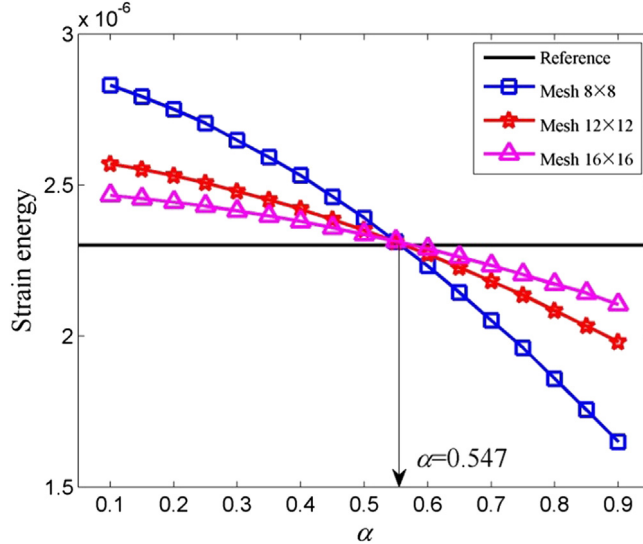


Fig. 9. The strain energy curves versus parameter α from different meshes for the pinched cylinder.

$\alpha \in [0, 1]$. Such a α is named as α_{exact} . It is clear that the nearly exact strain energy solutions can be achieved with $\alpha = \alpha_{\text{exact}}$. In addition, using $\alpha = \alpha_{\text{exact}}$ always results in very good displacement solution because the displacement solutions are linked to the strain energy solutions. However, it is known that α_{exact} is usually not easy to obtain because such a α not only has an dependence on the problem but also on the mesh style. In order to obtain nearly exact solution using HS-DSG3, a general procedure will be used to determine the value of α .

Property 6 (Easy to Implement). As discussed in Section 3, in practice, the implementation of HS-DSG3 is very similar to DSG3 and very simple. Therefore, the existing DSG3 code can be largely utilized.

4.7. Determination of α for a nearly exact solution

We have known that α_{exact} is not easy to find because both the problem and the mesh size are involved in this troublesome issue. The objective of the present work is to improve the accuracy of standard DSG3 and extend the application of H-GST from solid mechanics to shell analysis, hence a “preferable” α (α_{pre}), which is very close to α_{exact} , needs to be obtained to provide the nearly exact solutions. Here the procedure proposed in Ref. [62] is used directly to find the appropriate value of α . Although the proposed procedure is only a crude estimate for α and the obtained α may not be optimal. However, intensive numerical examples show that it is very effective and the resultant solutions are much better than the standard DSG3 and NS-DSG3 with the same mesh for shell structures.

5. Formulation of the geometrical nonlinear problems

In this paper, the modified Newton–Raphson method is used to solve the nonlinear equilibrium equation, then Eq. (23) can be rewritten as

$$\mathbf{g}(\mathbf{u}) = \mathbf{K}\mathbf{u} - \mathbf{F} = \mathbf{0}. \quad (83)$$

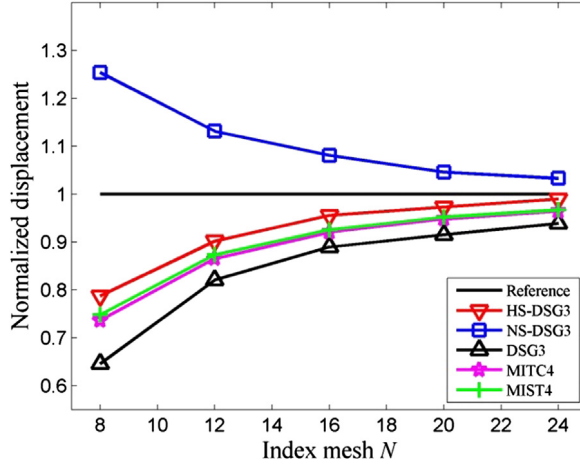


Fig. 10. The normalized displacements obtained using the different elements for the pinched cylinder.

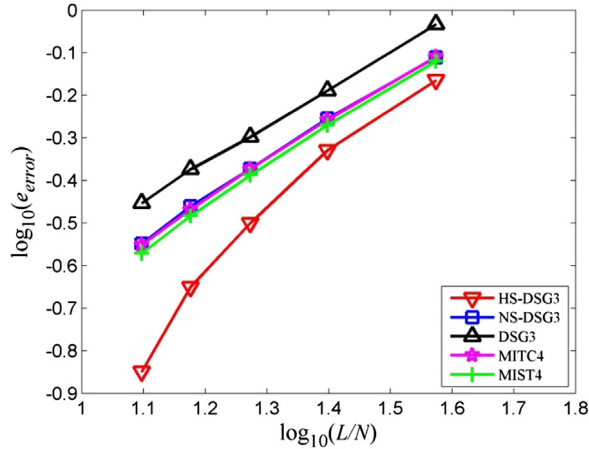


Fig. 11. The error in the strain energy norm from different elements for the pinched cylinder.

Assuming that the external load \mathbf{F} can be expressed as a function of the fixed load \mathbf{F}_0 , we have

$$\mathbf{F} = \lambda \mathbf{F}_0 \quad (84)$$

in which λ is the scale factor.

Then Eq. (83) can be rewritten as

$$\mathbf{g}(\mathbf{u}, \lambda) = \mathbf{K}\mathbf{u} - \lambda \mathbf{F}_0. \quad (85)$$

To obtain a new equilibrium state, both the scale factor λ and the displacement vector \mathbf{u} are updated by increments. Using the Taylor series, the following incremental form for Eq. (85) can be obtained.

$$\mathbf{g}(\mathbf{u} + \Delta\mathbf{u}, \lambda + \Delta\lambda) = \mathbf{g}(\mathbf{u}, \lambda) + \mathbf{K}_t \Delta\mathbf{u} - \Delta\lambda \mathbf{F}_0 = \mathbf{0} \quad (86)$$

in which $\Delta\lambda$ and $\Delta\mathbf{u}$ are the increments of the scale factor and the displacement vector, respectively, \mathbf{K}_t is the tangent stiffness matrix.

$$\mathbf{K}_t = \sum_{i=1}^{N_e} \mathbf{K}_{ti} = \sum_{i=1}^{N_e} (\mathbf{K}_i^l + \mathbf{K}_i^{nl} + \mathbf{K}_{gi}) \quad (87)$$

in which \mathbf{K}_{gi} denotes the element geometric stiffness matrix.

$$\mathbf{K}_{gi} = \int_{\Omega_e} \mathbf{G}^T \widehat{\mathbf{N}} \mathbf{G} d\Omega \quad (88)$$

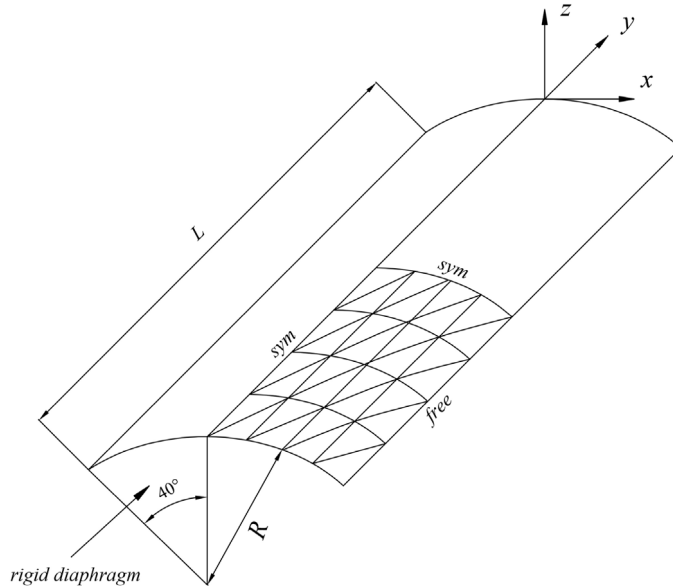


Fig. 12. The Scordelis-Lo roof under the self-weight (Poisson's ratio $\nu = 0$ and Young's modulus $E = 4.32 \times 10^8$).

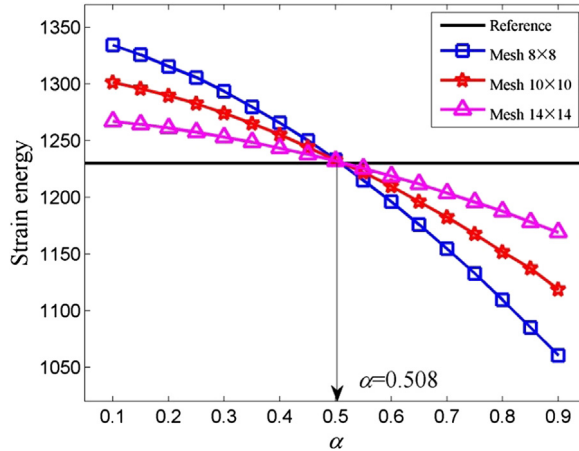


Fig. 13. The strain energy curves versus parameter α from different meshes for the roof.

where $\widehat{\mathbf{N}}$ is the membrane stress matrix and \mathbf{G} is given in Eq. (22).

$$\widehat{\mathbf{N}} = \begin{bmatrix} N_x & N_{xy} \\ N_{xy} & N_y \end{bmatrix} \quad (89)$$

in which N_x , N_y and N_{xy} are the membrane stress components given in Eq. (6).

To solve the nonlinear equation, the incremental-iterative method is used at each load step, then Eq. (86) can be expressed by the following form

$$[\mathbf{K}_t]_i \Delta \mathbf{u}_i^j = \Delta \lambda_i^j \mathbf{F}_0 - \mathbf{g}_i^{j-1} = \Delta \lambda_i^j \mathbf{F}_0 - \left[\mathbf{K}(\mathbf{u}_i^{j-1}) \mathbf{u}_i - \Delta \lambda_i^{j-1} \mathbf{F}_0 \right] \quad (90)$$

in which the subscript i and j are the load step number and the iteration cycle, respectively.

The incremental form of the displacement vector is given by

$$\Delta \mathbf{u}_i^j = [(\mathbf{K}_t)_i]^{-1} \left\{ \Delta \lambda_i^j \mathbf{F}_0 - \left[\mathbf{K}(\mathbf{u}_i^{j-1}) \mathbf{u}_i - \Delta \lambda_i^{j-1} \mathbf{F}_0 \right] \right\} = \Delta \lambda_i^j [\mathbf{u}_f]_i + [\Delta \mathbf{u}_r]_i^j. \quad (91)$$

From Eq. (60), it can be found that the increments of the displacement vector consists of two parts. The first part in Eq. (91) is related to the load increment and the second part in Eq. (91) is related to the residual force.

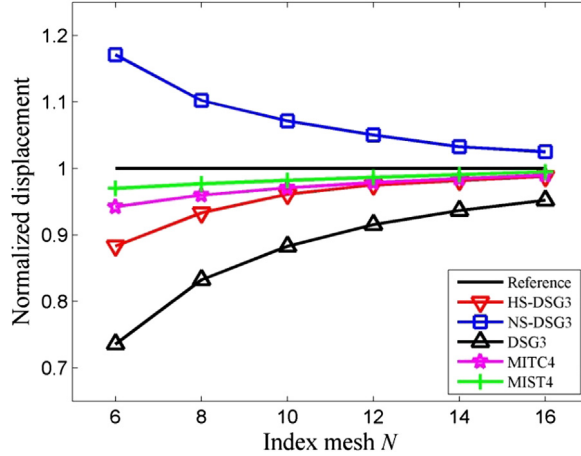


Fig. 14. The normalized displacements obtained using the different elements for the roof.

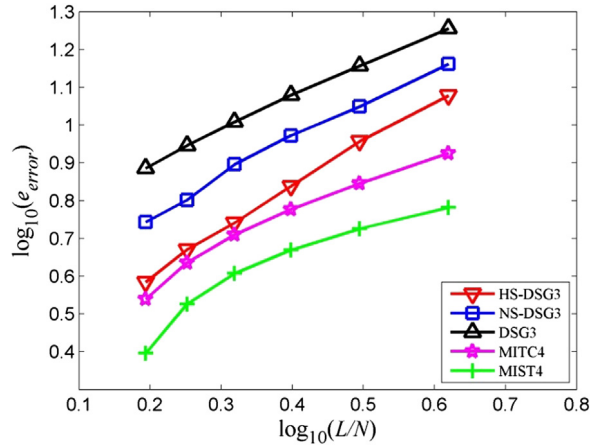


Fig. 15. The error in the strain energy norm from different numerical model for the roof.

In this paper, the increment of the external load is determined by using the arc-length method and the following convergence criterion is used.

$$\frac{\|\mathbf{g}(\mathbf{u}, \lambda)\|}{\|\mathbf{F}(\mathbf{u}, \lambda)\|} < \zeta \quad (92)$$

where ζ is the tolerance for convergence constant and it is set to 0.0001 in this work.

6. Numerical results

In this section, several typical numerical experiments are considered to assess the performance of the present method. For convenience of notation, the combined model presented in this work is named as HS-DSG3. To make a comparison, the numerical solutions from a number of other elements such as DSG3, NS-DSG3, MISTk (Mixed Interpolation with Smoothing Technique with $k \in [1, 2, 4]$) [70] and MITC (Mixed Interpolation of Tensorial Components) [12,71] are also presented in this paper.

6.1. Static analysis

With the aim to study the numerical solutions from different methods clearly, the strain energy error norm is used here. The strain energy error norm is defined by

$$e_{error} = |E_{num} - E_{exact}|^{1/2} \quad (93)$$

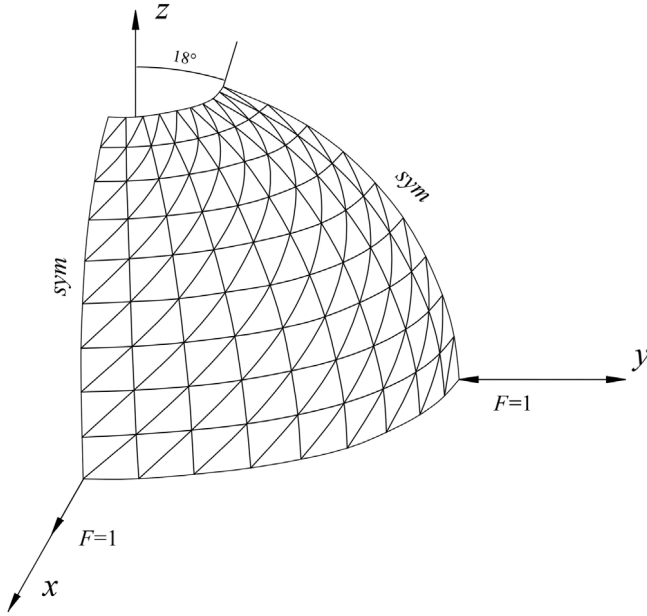


Fig. 16. A spherical shell under anti-symmetrical point load (Poisson's ratio $\nu = 0.3$, Young's modulus $E = 6.825 \times 10^7$).

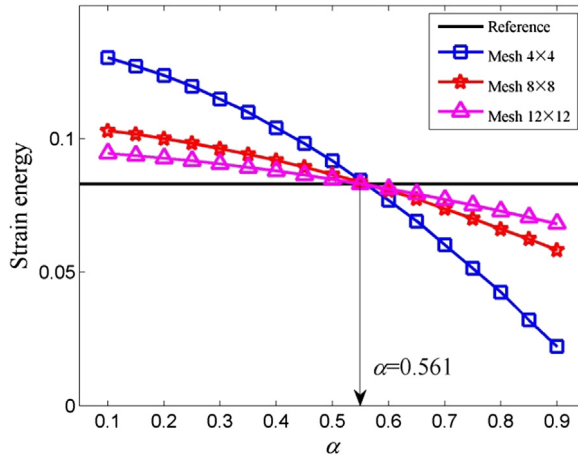


Fig. 17. The strain energy curves versus parameter α from different meshes for the spherical shell.

in which E_{exact} and E_{num} represents the exact strain energy and the strain energy from numerical methods, respectively. In practical computation, a high quality mesh will be used to obtain the “exact” strain energy.

6.1.1. Example 1: The pinched cylinder under point load

The cylindrical shell (length $L = 600$, thickness $t = 3$ and $R = 300$) under a point load shown in Fig. 8 is firstly studied as benchmark problem. The rigid diaphragms are at its ends and the point load $P = 1$ is at the center of its surface. Using the symmetry condition, only one eighth of the cylinder is modeled. The $2 \times N \times N$ ($N = 8, 12, 16, 20, 24$) triangular meshes are used to discretize the cylindrical shell here. This benchmark problem has been investigated many times before and the reference solution of the deformation at the center of the cylinder is 1.8425×10^{-5} [72]. The following numerical solutions are normalized with this value.

We have known that the stiffness of NS-DSG3 is always softer than the exact stiffness of the continuous system and the DSG3 is always stiffer than the exact one, hence the numerical solutions of the present HS-DSG3, which is exactly a combination of NS-DSG3 and DSG3, usually lie in between the NS-DSG3 solutions and the DSG3 solutions. Actually, the value of α is of quite importance to ensure the quality of the HS-DSG3 solutions because the contribution proportions of NS-DSG3 and DSG3 to the combined model are controlled by the value of α .

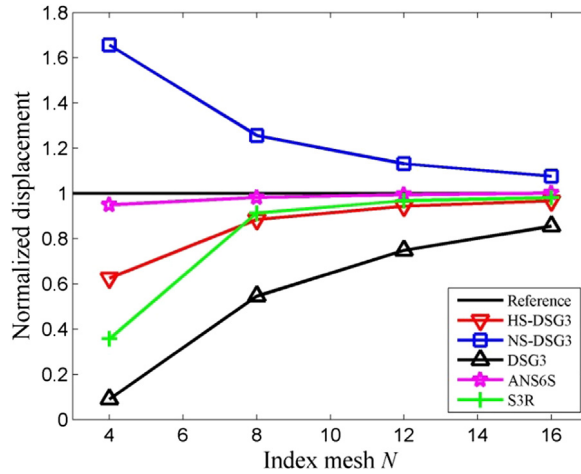


Fig. 18. The normalized displacements obtained using the different elements for spherical shell.

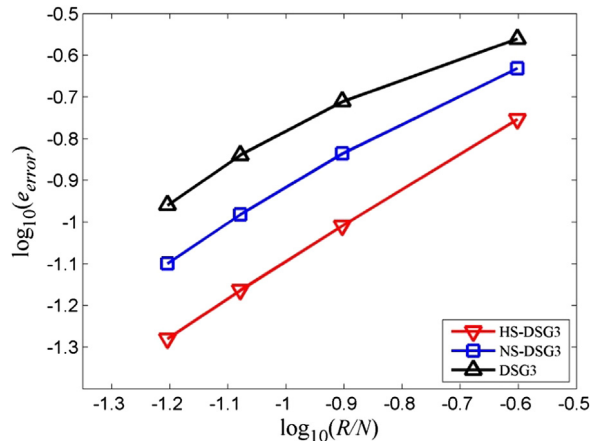


Fig. 19. The error in the strain energy norm from different numerical models for the spherical shell.

Therefore, for the present HS-DSG3 model for shell analysis, the first step is to find the preferable α (α_{pre}). Following the procedure proposed in Ref. [62], the strain energy curves of three different meshes are plotted in Fig. 9. From the figure, it is found that all the energy curves will approximately intersect at one point. Therefore, it may be reasonable to choose the preferable α to be $\alpha_{\text{pre}} = 0.547$ and then this value of α will be used in the computation for this particular problem.

The normalized displacement solutions of the HS-DSG3 together with the numerical results from other shell elements such as MITC4, MIST4, NS-DSG3 and DSG3 elements are shown Fig. 10. We can observe that the present HS-DSG3 solutions lie in between the NS-DSG3 and DSG3. However, HS-DSG3 can achieve much more accurate results than either DSG3 or NS-DSG3 elements and even better than the MITC4 and MIST4 elements.

Besides, Fig. 11 plots the error in the strain energy norm from different elements, it is clear that the HS-DSG3 solutions are much more accurate than NS-DSG3 and DSG3 solutions. What is more, the present HS-DSG3 even behaves better than the MITC4 and MIST4 with quadrilateral elements. These findings demonstrate that the individual advantages of NS-DSG3 and DSG3 have been largely used by the combined model and the present HS-DSG3 usually possesses a relatively proper stiffness. Therefore, very accurate numerical solutions could be obtained from the HS-DSG3. In addition, we find that the thickness ($t/L = 0.005$) of the pinched cylinder considered here is very small. It is also demonstrated that the HS-DSG3 can successfully overcome the shear locking issue because the discrete shear gap technique is used.

6.1.2. Example 2: The Scordelis–Lo roof under uniform load

The second numerical example (see Fig. 12) considered here is the well-known Scordelis–Lo roof (thickness $t = 0.25$, length $L = 50$ and the radius $R = 25$). Two straight edges of the cylindrical concrete roof are free and the remaining curved edges are simply supported. The external load is the self-weight of the roof $q = 90$ per unit area. This benchmark problem

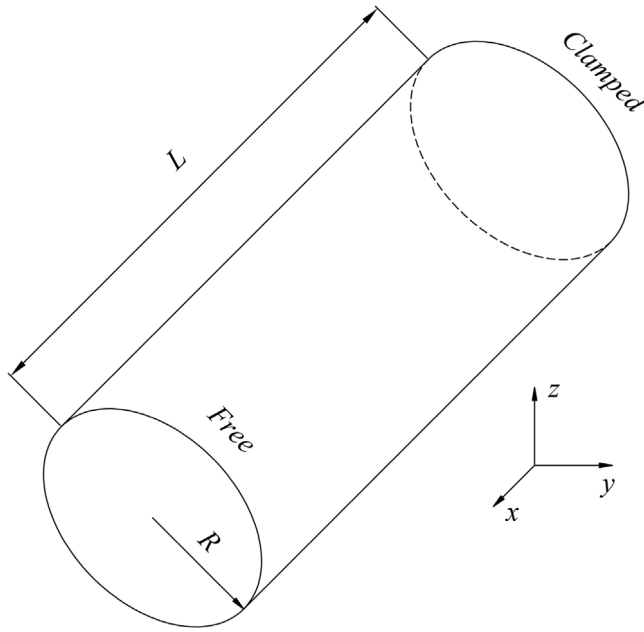


Fig. 20. The geometry of the cylindrical shell (the mass density $\rho = 7800$, Poisson's ratio $\nu = 0.3$ and Young's modulus $E = 2.1 \times 10^{11}$).

was first modeled by MacNeal and Harder and the reference solution of the vertical displacement of the mid-edge-point is 0.3024 [73]. Only a quarter of the roof is needed to model due to the symmetry. A series of regular mesh of $2 \times N \times N$ three-node triangular elements with $N = 6, 8, 10, 12, 14, 16$ are used in the actual computation. Following the procedure mentioned in previous section, the strain energy curves versus the parameter α are depicted in Fig. 13. The preferable α is found to be $\alpha_{\text{pre}} = 0.508$ from the figure for this particular problem.

The comparison of the normalized displacement results of the HS-DSG3 with the DSG3, NS-DSG3, MITC4 and MIST4 are shown Fig. 14. From the figure, we can find that the DSG3 model is always "overly-stiff" and the NS-DSG3 is always "overly-soft". Therefore, compared to the reference solutions obtained from a very fine mesh, the NS-DSG3 solutions are always larger and the DSG3 solutions are always smaller than the reference ones. However, the solutions of the present HS-DSG3 solutions are more closer to the reference solutions. Though the HS-DSG3 solutions are not as good as those from the MITC4 and MIST4 elements in which the quadrilateral elements are used, the performance of the DSG3 and NS-DSG3 has been improved significantly by the present HS-DSG3.

Besides, we also calculate the error in the strain energy norm from different numerical model for the Scordelis–Lo roof and the results are shown in Fig. 15. From the figure, we can find that the HS-DSG3 solutions are not better than MITC4 and MIST4, however, the HS-DSG3 solutions are much better than either DSG3 or NS-DSG3 and the higher convergence rate of the strain energy can be achieved. From this numerical example, we can conclude again that the present HS-DSG3 model has a proper stiffness of the continuous system, hence it could produce fairly accurate solutions.

6.1.3. Example 3: The spherical shell with an 18° hole under anti-symmetrical unit load

Furthermore, the spherical shell problem with an 18° hole (thickness $t = 0.04$ and radius $R = 10$) under anti-symmetrical point load $F = 1$ is considered here (see Fig. 16). The inner of the hole is free boundary condition and other edges are symmetric boundary conditions. This benchmark problem are also studied many times before and the referential radial displacement solution at load is 0.0924 [73]. Four regular meshes with $2 \times N \times N$ elements ($N = 4, 8, 12, 16$) are used in practical computation. Following the procedure mentioned in Section 4.7, the strain energy curves versus parameter α from different meshes for this problem are shown in Fig. 17. From the figure, the preferable α is found to be $\alpha_{\text{pre}} = 0.561$ for this particular problem.

Fig. 18 shows the normalized radial displacement results at load from different numerical models. In order to give a comparison, the results from DSG3, NS-DSG3, ANS6S [74] and S3R [75] are also presented in the figure. It is clear that the HS-DSG3 solutions are in good agreement with the ANS6S and S3R results, more importantly, HS-DSG3 still behaves much better than DSG3 and NS-DSG3. Moreover, the convergence of the strain energy from different numerical models for the spherical shell are plotted in Fig. 19. From the plot, similar conclusions found in the previous sections can be drawn and it is demonstrated that the present HS-DSG3 behaves much better than DSG3 and is capable of handling the shell structures with very complicated geometries.

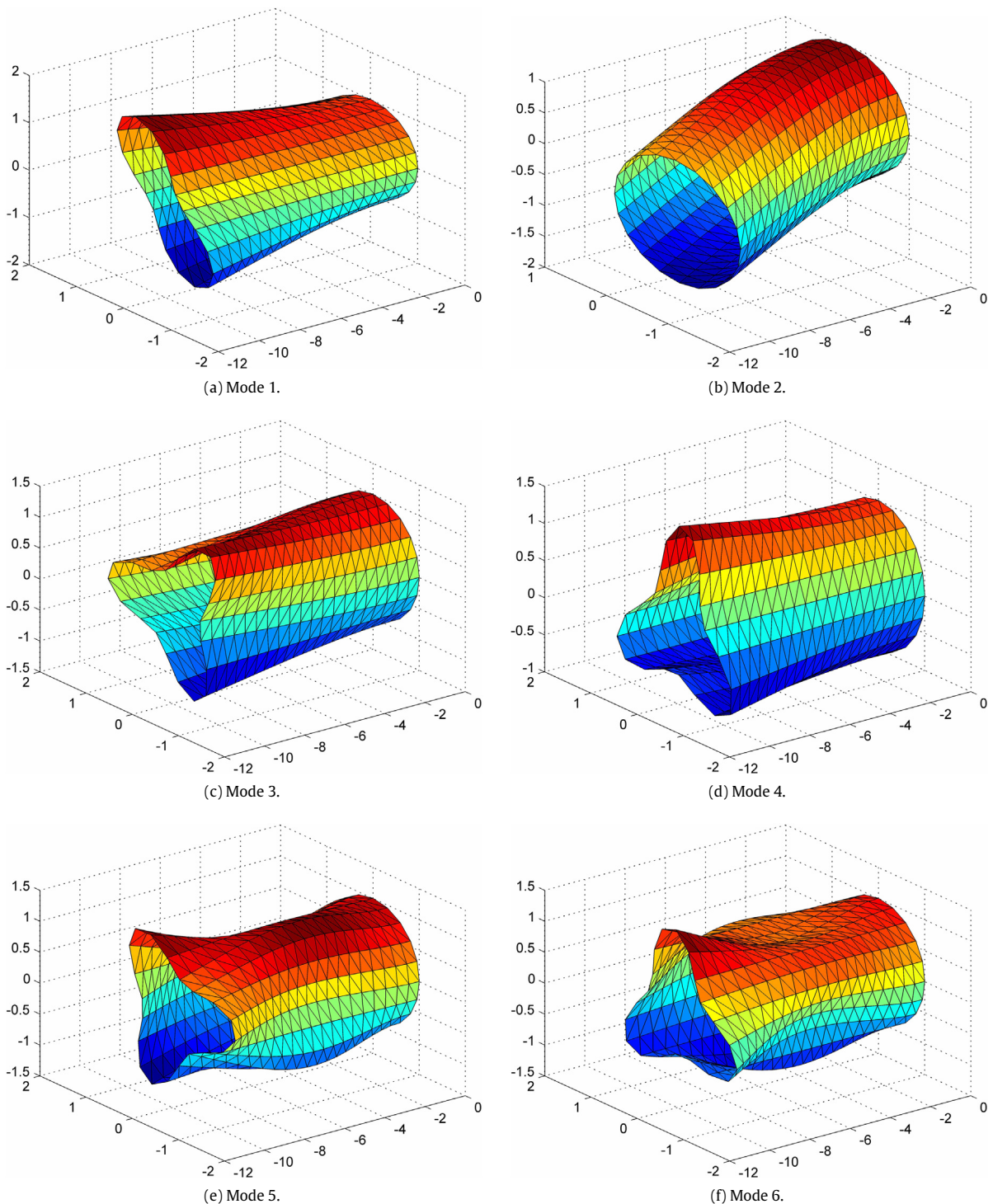


Fig. 21. The first to sixth modes of the cylindrical shell from the HS-DSG3.

6.2. Free vibration analysis

In this section, two typical numerical examples are given to examine the performance of the present HS-DSG3 formulation in free vibration analysis. From the results presented in previous section, it is observed that the value of the preferable α varies

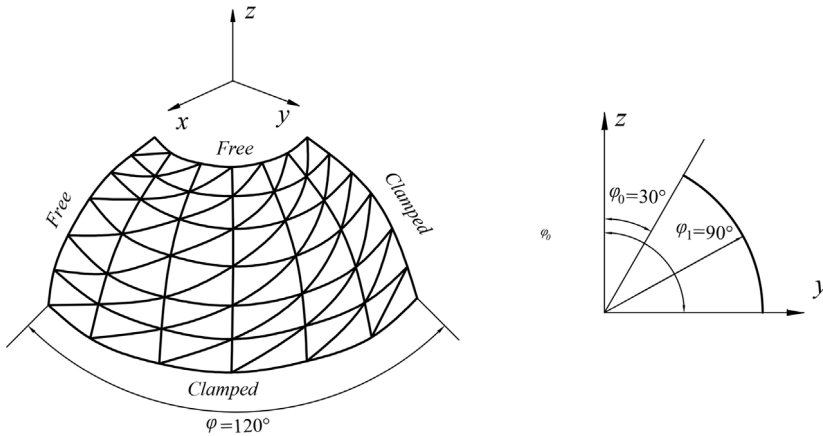


Fig. 22. The geometry of a hemispherical panel (the mass density $\rho = 7800$, Poisson's ratio $\nu = 0.3$ and Young's modulus $E = 2.1 \times 10^{11}$).

Table 1
Comparison of non-dimensional frequency parameter $\bar{\omega}$ for the cylindrical shell.

Mesh	Method	Mode							
		1	2	3	4	5	6	7	8
8×8	DKT	1.472	1.489	2.390	2.402	3.096	3.174	6.194	6.524
	MITC4	1.339	1.344	2.206	2.214	4.168	4.250	5.305	5.375
	MIN3	1.805	1.811	2.393	2.406	3.694	3.819	6.784	6.858
	DSG3	1.543	1.560	2.390	2.403	4.235	4.322	6.709	6.825
	CS-DSG3	1.456	1.475	2.390	2.402	2.962	3.006	5.748	5.971
	HS-DSG3	1.346	1.365	2.203	2.208	3.946	4.059	5.957	5.978
12×12	DKT	1.253	1.256	2.303	2.306	2.649	2.662	4.549	4.578
	MITC4	1.188	1.189	2.213	2.214	2.926	2.936	4.013	4.025
	MIN3	2.007	2.014	2.312	2.315	4.005	4.044	5.556	5.556
	DSG3	1.281	1.285	2.303	2.306	2.989	2.998	4.786	4.814
	CS-DSG3	1.249	1.253	2.303	2.306	2.621	2.628	4.539	4.571
	HS-DSG3	1.156	1.161	2.211	2.212	2.568	2.601	4.068	4.086
16×16	DKT	1.176	1.177	2.269	2.270	2.469	2.473	3.884	3.893
	MITC4	1.138	1.138	2.216	2.216	2.598	2.601	3.586	3.590
	MIN3	2.286	2.287	2.399	2.403	4.666	4.684	5.464	5.471
	DSG3	1.191	1.192	2.269	2.270	2.632	2.634	4.003	4.012
	CS-DSG3	1.175	1.176	2.269	2.270	2.463	2.465	3.883	3.893
	HS-DSG3	1.112	1.114	2.215	2.215	2.367	2.378	3.549	3.556
20×20	DKT	1.140	1.140	2.252	2.253	2.383	2.384	3.593	3.596
	MITC4	1.115	1.115	2.217	2.217	2.459	2.460	3.403	3.405
	MIN3	2.279	2.279	2.845	2.848	5.443	5.452	5.534	5.535
	DSG3	1.149	1.150	2.253	2.253	2.479	2.480	3.665	3.669
	CS-DSG3	1.139	1.140	2.252	2.253	2.383	2.384	3.593	3.597
	HS-DSG3	1.096	1.097	2.216	2.216	2.302	2.307	3.356	3.359
Leissa		1.109	–	2.458	–				
RSQ20		1.092	1.092	2.237	2.237				
RSQ24		1.101	1.101	2.237	2.277				

approximately in the interval of 0.5–0.6. Here, we directly choose the parameter $\alpha_{\text{pre}} = 0.55$ for free vibration and geometric nonlinear analysis of the shell structures. Although this value of α may not be optimal for all the numerical examples, it is found that the resultant solutions are still better than the DSG3 and NS-DSG3. For comparison, the solutions calculated using other numerical models such as DKT [76], MIN3 [77], MTC4 [12,71], DSG3 and CS-DSG3 [78] are also available in this paper.

6.2.1. Example 1: The cylindrical shell problem

A cylindrical shell with length to radius ratio $L/R = 10$ and radius to thickness ratio $R/t = 100$ is considered here. As shown in Fig. 20, one end of the cylindrical is clamped and the other end is free. The natural frequencies of the cylindrical shell are studied here and a non-dimensional frequency parameter defined by $\bar{\omega} = 100\omega R\sqrt{\rho(1-\nu^2)/E}$ (ω denotes angular frequency) is employed. A series of $2 \times N \times N$ regular meshes ($N = 8, 12, 16, 20$) are used in this numerical example. Table 1 presents the eight lowest non-dimensional frequency results from different elements for the cylindrical shell. From the table, it is clear that all the results from different elements are in complete accord with the reference solutions by Leissa [79] and the RSQ20 and RSQ24 results [80] for low mode orders. However, all the numerical solutions from different elements will

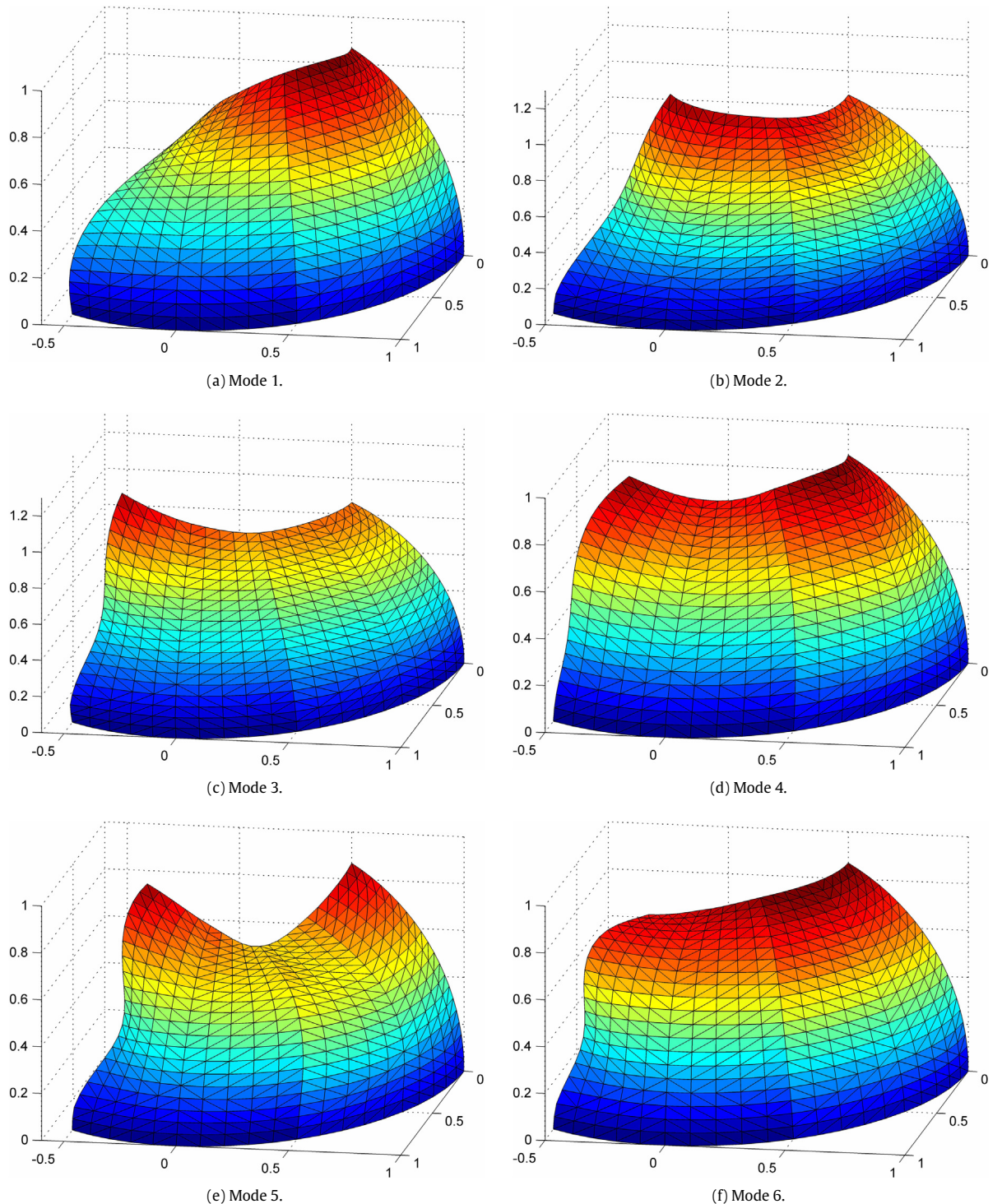


Fig. 23. The first to sixth modes of the hemispherical panel from the HS-DSG3.

gradually deviate from the reference solutions with the increase of the mode order. Nevertheless, the HS-DSG3 solutions are much better than the DSG3 solutions. What is more, it should be pointed out that the present HS-DSG3 behaves even better than the CS-DSG3 and MITC4. Moreover, Fig. 21 shows the first to sixth modes of the cylindrical shell obtained from

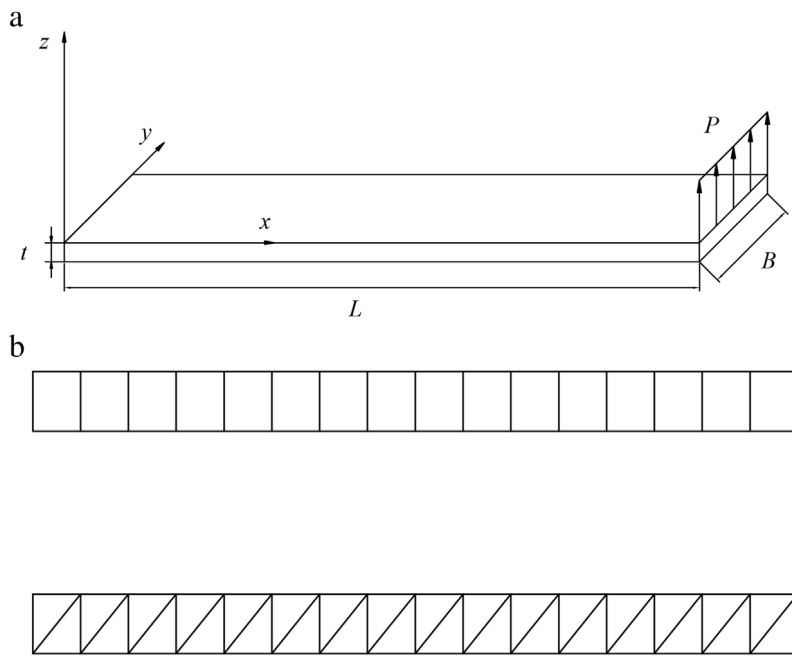


Fig. 24. The cantilever plate under end shear force (Poisson's ratio $\nu = 0$ and Young's modulus $E = 2 \times 10^{11}$). (a) Geometry configuration. (b) Mesh patterns.

Table 2
Numerical results of natural frequency for the hemispherical panel.

Mesh	Method	Mode							
		1	2	3	4	5	6	7	8
8×8	DKT	359.3	496.4	777.5	1009	1178	1465.2	1506.5	1671.3
	MITC4	332.5	471.3	729	950.7	1102.9	1392.7	1420.6	1520.9
	MIN3	771	890.7	1273.8	1558.9	1810	1932.6	1980.5	2043.1
	CS-DSG3	346.3	472.4	750.6	983.4	1136.4	1378.1	1450.1	1585.1
	HS-DSG3	331.17	430.95	725.64	899.98	1066	1113.3	1340.1	1427.6
12×12	DKT	350.6	487.1	755.1	960.8	1130.8	1398.7	1451.3	1566.9
	MITC4	328.9	464.5	715.7	917.3	1073.4	1334.5	1367	1447.4
	MIN3	809.4	931.3	1329.9	1586	1817.2	1906.1	2004	2116.4
	CS-DSG3	338.3	467	731.6	933.03	1089.6	1346.1	1368.2	1475.6
16×16	HS-DSG3	330.61	438.28	727.62	901.55	1079.7	1109.8	1301.6	1405.3
	DKT	346.4	483.2	745	942	1113.3	1368.4	1429.8	1529.5
	MITC4	328	462.6	711.5	906.1	1064.4	1311.5	1349.5	1424.1
	MIN3	831.2	954.8	1359.6	1612.1	1851.9	1911.7	2039.4	2175.1
	CS-DSG3	334.4	464.1	722.4	913.7	1071.8	1329.1	1331.4	1436.2
20×20	HS-DSG3	330.12	450.68	732.25	901.53	1084	1124.4	1290.9	1383.7
	DKT	344.2	481.2	739.7	932.8	1105	1352.6	1419.3	1512.8
	MITC4	327.7	461.8	709.7	901.1	1060.7	1300.7	1342	1414.2
	MIN3	844.6	969.8	1376	1630.8	1882.5	1925.1	2068.3	2219.4
	CS-DSG3	332.2	462.4	717.3	904.1	1063.2	1309.2	1323.1	1417.6
	HS-DSG3	329.9	449.03	730.85	900.02	1078	1126.6	1281.2	1379.9
	Abaqus	326.94	459.01	706.98	884.09	1047.6	1270.8	1309.2	1383.7
	Ansys	328.48	460.89	710.52	893.51	1056.1	1285.2	1328	1404
	Nastran	328.69	460.93	711.09	892.71	1055.8	1282.4	1325.9	1401.9
	Straus	327.28	458.54	706.64	888.86	1049.5	1278.9	1313.9	1395.5
	GDQ	327.39	458.58	705.71	885.18	1046.6	1270.7	1305.1	1382.8

HS-DSG3. We can find that the present HS-DSG3 model is very stable and shows good behaviors for free vibration analysis of shell structures.

6.2.2. Example 2: A hemispherical panel

In this sub-section a benchmark problem of a hemispherical panel with two clamped edges and two free edges is studied to assess the performance of the proposed HS-DSG3. As illustrated in Fig. 22, the geometric parameters are thickness $t = 0.1$ m and radius $R = 1$ m, $\varphi_0 = 30^\circ$, $\varphi_1 = 90^\circ$, $\varphi = 120^\circ$, two edges of the hemispherical shell are clamped and

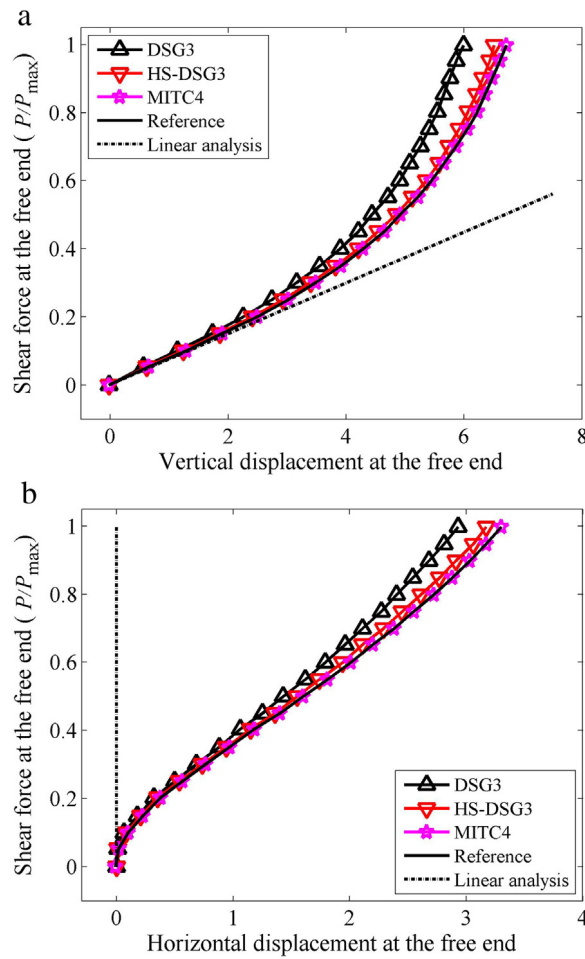


Fig. 25. The end shear force versus the displacement results of the cantilever plate. (a) The vertical displacement results. (b) The horizontal displacement results.

the other two edges are free. The $2 \times N \times N$ regular meshes with $N = 8, 12, 16, 20$ are used here. Table 2 shows the first to eighth natural frequency results of the hemispherical shell with the different elements. In order to give a comparison, the results from the generalized differential quadrature (GDQ) method are chosen to be the reference solutions [81]. In addition, the corresponding results from several commercial software packages (Nastran, Ansys, Abaqus and Straus) [78] are also listed in Table 2. From the table, it is found that the present HS-DSG3 model shows superior performance in free vibration analysis of shell structures. Fig. 23 shows the first to sixth modes of the hemispherical panel and it is clear that all the modes express exactly the real physical modes of the shell.

6.3. Geometric nonlinear analysis

In this section, two typical benchmark problems will be considered to assess the performance of the present method in geometric nonlinear analysis. For nonlinear analysis, it is generally difficult to obtain the “exact” α for all loading stages. Similarly to the free vibration problems, $\alpha = 0.55$ is used here. The numerical tests so far shown that the using of such an α can usually provide more accurate results than the DSG3. Of course, the α chosen here is not optimal for the nonlinear problem and we will not obtain a nearly exact solution, but the accuracy of the DSG3 solution is still significantly improved.

6.3.1. Example 1: The cantilever plate under shear force

The cantilever plate (length $L = 10$, width $B = 1$ and thickness $t = 0.1$) under end shear force is considered (see Fig. 24). This is a very popular benchmark problem for nonlinear analysis of shell structures [82,83]. The maximum value of the external shear force is $P_{\max} = 4$. The end shear force versus the numerical solutions of the displacements are shown in Fig. 25. For comparison, all the numerical solutions from different shell elements are plotted in the figure. The reference solutions are the numerical results using high quality meshes. From the results we can find that: although the present

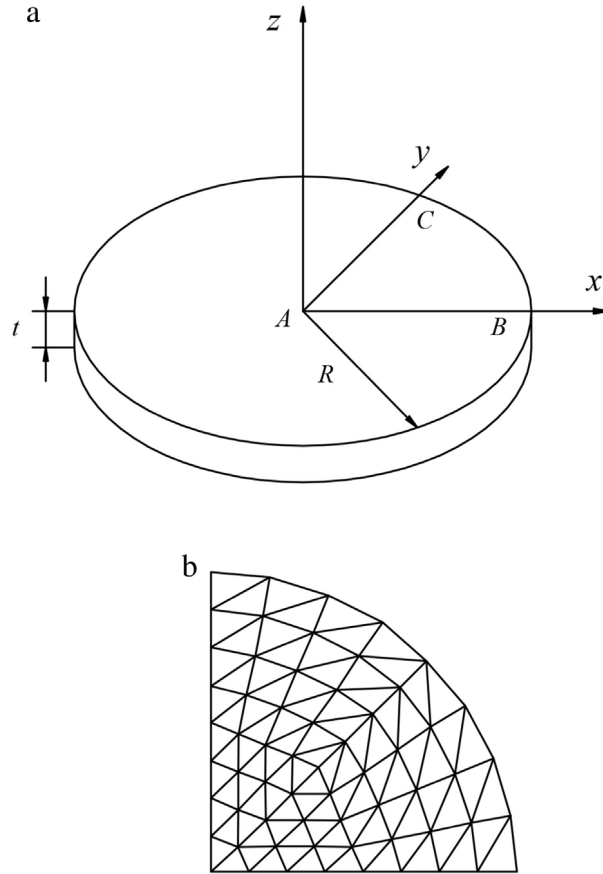


Fig. 26. The circular plate with clamped boundary condition (Poisson's ratio $\nu = 0.3$ and Young's modulus $E = 3 \times 10^7$). (a) The geometry configuration. (b) The mesh pattern.

HS-DSG3 does not behave as well as the well-known MITC4 elements, the performance of the original DSG3 has been improved significantly.

6.3.2. Example 2: The clamped circular plate

Another numerical example for geometric nonlinear analysis is the circular plate (radius $R = 1$ and thickness $t = 0.1$) under uniform load with clamped boundary condition (see Fig. 26). The maximum value of the uniform load is $q_{\max} = 220$. Only one quarter of the plate is needed to model in practical computation owing to the symmetry property of the plate. The analytical solution to this problem is given by [84]:

$$\frac{qR^4}{Et^4} = \frac{16}{3(1-\nu^2)} \left[\frac{w}{t} + \frac{1}{360} (1+\nu) (173 - 73\nu) \left(\frac{w}{t} \right)^3 \right] \quad (94)$$

where w is the central deflection of the plate.

The uniform load versus the vertical displacement at the center of the plate are depicted in Fig. 27. From the plot, we can find that the present HS-DSG3 solutions are more accurate than the DSG3 solutions. What is more, the HS-DSG3 even behaves slightly better than ES-DSG3 which has been proved to be very effective for plates and shells [75]. Therefore, we can again conclude that the HS-DSG3 is sufficiently effective for nonlinear shell analysis and the performance of the original DSG3 has been improved significantly.

7. Conclusions

In this paper, the coupling of hybrid gradient smoothing technique (H-GST) and the DSG using triangular elements (HS-DSG3) is presented to analyze shell structures. From the numerical examples, the following points can be obtained:

- (a) In the HS-DSG3 model, a scale factor α is introduced to control the contributions from the NS-DSG3 and DSG3. Then a continuous solution function from NS-DSG3 solutions to DSG3 solutions can be obtained by varying the value of α from 0 to

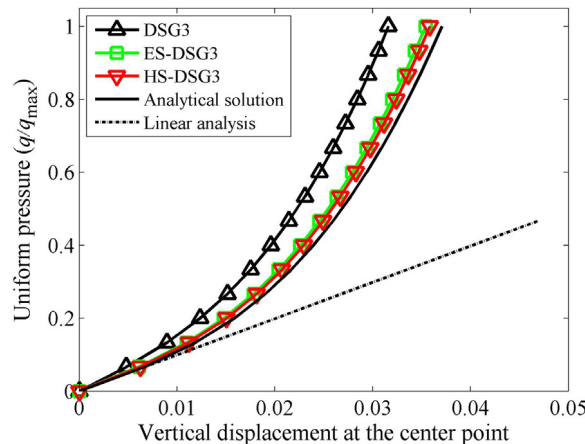


Fig. 27. The uniform load versus the vertical displacement results for the clamped circular plate.

1. By using a proper α , the present HS-DSG3 model could provide a “close-to-exact” stiffness of the continuous system and achieve better solutions than DSG3.

(b) For linear and nonlinear analysis, the present HS-DSG3 can even provide better solutions than the ES-DSG3, which has been proved to be a high convergent element for plates and shells. Therefore, the HS-DSG3 can be a very good alternative method for shell analysis.

(c) For free vibration analysis, the “overly-soft” property of the original NS-DSG3 model has been overcome successfully by the present HS-DSG3 model and no spurious non-zero-energy modes can be obtained.

(d) Since only triangular elements, which have significant advantages over other elements for complicated domains, are required in the present HS-DSG3 model, hence the HS-DSG3 has great potential in practical engineering applications.

Acknowledgment

This work was supported by the National Natural Science Foundation of China (grant numbers: 51579112, 51379083 and 51579109).

References

- [1] O.C. Zienkiewicz, R.L. Taylor, *The Finite Element Method for Solid and Structural Mechanics*, Butterworth-heinemann, 2005.
- [2] D.E. Beskos, *Boundary Element Analysis of Plates and Shells*, Springer Science & Business Media, 2012.
- [3] N.H. Kim, K.K. Choi, J.S. Chen, M.E. Botkin, Meshfree analysis and design sensitivity analysis for shell structures, *Internat. J. Numer. Methods Engrg.* 53 (2002) 2087–2116.
- [4] P. Krysl, T. Belytschko, Analysis of thin shells by the element-free Galerkin method, *Int. J. Solids Struct.* 33 (1996) 3057–3080.
- [5] F. Tornabene, N. Fantuzzi, M. Bacciochi, E. Viola, J.N. Reddy, A numerical investigation on the natural frequencies of FGM sandwich shells with variable thickness by the local generalized differential quadrature method, *Appl. Sci.* 7 (2017) 131.
- [6] F. Tornabene, N. Fantuzzi, M. Bacciochi, On the mechanics of laminated doubly-curved shells subjected to point and line loads, *Internat. J. Engrg. Sci.* 109 (2016) 115–164.
- [7] F. Tornabene, N. Fantuzzi, M. Bacciochi, The GDQ method for the free vibration analysis of arbitrarily shaped laminated composite shells using a NURBS-based isogeometric approach, *Compos. Struct.* 154 (2016) 190–218.
- [8] M. Bacciochi, M. Eisenberger, N. Fantuzzi, F. Tornabene, E. Viola, [ibration analysis of variable thickness plates and shells by the Generalized Differential Quadrature method, *Compos. Struct.* 156 (2016) 218–237.
- [9] J.N. Reddy, *Theory and Analysis of Elastic Plates and Shells*, CRC Press, Taylor and Francis Group, NewYork, 2006.
- [10] T.J.R. Hughes, M. Cohen, M. Haroun, Reduced and selective integration techniques in the finite element analysis of plates, *Nucl. Eng. Des.* 46 (1978) 203–222.
- [11] E.N. Dvorkin, K.J. Bathe, A continuum mechanics based four-node shell element for general non-linear analysis, *Eng. Comput.* 1 (1984) 77–88.
- [12] K.J. Bathe, E.N. Dvorkin, A formulation of general shell elements—the use of mixed interpolation of tensorial components, *Internat. J. Numer. Methods Engrg.* 22 (1986) 697–722.
- [13] R.H. Macneal, Derivation of element stiffness matrices by assumed strain distributions, *Nucl. Eng. Des.* 70 (1982) 3–12.
- [14] K.U. Bletzinger, M. Bischoff, E. Ramm, A unified approach for shear-locking-free triangular and rectangular shell finite elements, *Comput. Struct.* 75 (2000) 321–334.
- [15] G.R. Liu, On G space theory, *Int. J. Comput. Methods* 6 (2009) 257–289.
- [16] M. Chen, M. Li, G.R. Liu, Mathematical basis of G spaces, *Int. J. Comput. Methods* 13 (2016) 1641007.
- [17] G.R. Liu, G.Y. Zhang, *Smoothed Point Interpolation Methods: G Space Theory and Weakened Weak Forms*, World Scientific, 2013.
- [18] G.R. Liu, G.Y. Zhang, A normed G space and weakened weak (W^2) formulation of cell-based smoothed point interpolation method, *Int. J. Comput. Methods* 6 (2009) 147–179.
- [19] G.R. Liu, T. Nguyen-Thoi, *Smoothed Finite Element Method*, Taylor and Francis Group, New York, CRC Press, 2010.
- [20] W. Zeng, G.R. Liu, Smoothed finite element methods (S-FEM): An overview and recent developments, *Arch. Comput. Methods Eng.* (2016) 1–39.

- [21] G.R. Liu, K.Y. Dai, T. Nguyen-Thoi, A smoothed finite element method for mechanics problems, *Comput. Mech.* 39 (2007) 859–877.
- [22] G.R. Liu, T. Nguyen-Thoi, K.Y. Dai, K.Y. Lam, Theoretical aspects of the smoothed finite element method (SFEM), *Internat. J. Numer. Methods Engrg.* 71 (2007) 902–930.
- [23] G.R. Liu, W. Zeng, H. Nguyen-Xuan, Generalized stochastic cell-based smoothed finite element method (GS-CS-FEM) for solid mechanics, *Finite Elem. Anal. Des.* 63 (2013) 51–61.
- [24] W. Zeng, G.R. Liu, C. Jiang, T. Nguyen-Thoi, Y. Jiang, A generalized beta finite element method with coupled smoothing techniques for solid mechanics, *Eng. Anal. Bound. Elem.* 73 (2016) 103–119.
- [25] W. Zeng, G.R. Liu, C. Jiang, X.W. Dong, H.D. Chen, Y. Bao, Y. Jiang, An effective fracture analysis method based on the virtual crack closure-integral technique implemented in CS-FEM, *Appl. Math. Model.* 40 (2016) 3783–3800.
- [26] W. Li, Y.B. Chai, M. Lei, G.R. Liu, Analysis of coupled structural-acoustic problems based on the smoothed finite element method (S-FEM), *Eng. Anal. Bound. Elem.* 42 (2014) 84–91.
- [27] Y. Li, M. Li, G.R. Liu, A modified triangulation algorithm tailored for the smoothed finite element method (S-FEM), *Int. J. Comput. Methods* 11 (2014) 1350069.
- [28] T. Nguyen-Thoi, P. Phung-Van, T. Rabczuk, H. Nguyen-Xuan, C.V. Le, Free and forced vibration analysis using the n-sided polygonal cell-based smoothed finite element method (nCS-FEM), *Int. J. Comput. Methods* 10 (2013) 1340008.
- [29] Y. Li, G.Y. Zhang, G.R. Liu, Y.N. Huang, Z. Gong, A contact analysis approach based on linear complementarity formulation using smoothed finite element methods, *Eng. Anal. Bound. Elem.* 37 (2013) 1244–1258.
- [30] D.T. Wan, D. Hu, G. Yang, T. Long, A fully smoothed finite element method for analysis of axisymmetric problems, *Eng. Anal. Bound. Elem.* 72 (2016) 78–88.
- [31] W. Li, X.Y. You, Y.B. Chai, T.Y. Li, Edge-based smoothed three-Node Mindlin plate element, *J. Eng. Mech.* (2016) 04016055.
- [32] Y.T. Yang, H. Zheng, X.L. Du, An enriched edge-based smoothed fem for linear elastic fracture problems, *Int. J. Comput. Methods* 14 (2016) 1750052.
- [33] Y.B. Chai, W. Li, Z.X. Gong, T.Y. Li, Hybrid smoothed finite element method for two dimensional acoustic radiation problems, *Appl. Acoust.* 103 (2016) 90–101.
- [34] H. Nguyen-Xuan, G.R. Liu, C. Thai-Hoang, T. Nguyen-Thoi, An edge-based smoothed finite element method (ES-FEM) with stabilized discrete shear gap technique for analysis of Reissner–Mindlin plates, *Comput. Methods Appl. Mech. Engrg.* 199 (2010) 471–489.
- [35] Y.B. Chai, W. Li, G.R. Liu, Z.X. Gong, T.Y. Li, A superconvergent alpha finite element method (S α FEM) for static and free vibration analysis of shell structures, *Comput. Struct.* 179 (2017) 27–47.
- [36] J. Liu, Z.Q. Zhang, G.Y. Zhang, A smoothed finite element method (S-FEM) for large-deformation elastoplastic analysis, *Int. J. Comput. Methods* 12 (2015) 1540011.
- [37] X.Y. Cui, X.B. Hu, G.Y. Li, G.R. Liu, A modified smoothed finite element method for static and free vibration analysis of solid mechanics, *Int. J. Comput. Methods* 3 (2016) 1650043.
- [38] X. Zhao, G.R. Liu, K.Y. Dai, Z.H. Zhong, G.Y. Li, X. Han, Free-vibration analysis of shells via a linearly conforming radial point interpolation method (LC-RPIM), *Finite Elem. Anal. Des.* 45 (2009) 917–924.
- [39] G. Wu, J. Zhang, Y.L. Li, L.R. Yin, Z.Q. Liu, Analysis of transient thermo-elastic problems using a cell-based smoothed radial point interpolation method, *Int. J. Comput. Methods* 13 (2016) 1650023.
- [40] X. Xu, Z.Q. Zhang, Y.T. Gu, G.R. Liu, A quasi-conforming point interpolation method (QC-PIM) for elasticity problems, *Int. J. Comput. Methods* 13 (2016) 1650026.
- [41] J.H. Yue, M. Li, G.R. Liu, R.P. Niu, Proofs of the stability and convergence of a weakened weak method using PIM shape functions, *Comput. Math. Appl.* 72 (2016) 933–951.
- [42] Y.O. Zhang, T. Zhang, H. Ouyang, T.Y. Li, Efficient SPH simulation of time-domain acoustic wave propagation, *Eng. Anal. Bound. Elem.* 62 (2016) 112–122.
- [43] Y.O. Zhang, T. Zhang, H. Ouyang, T.Y. Li, SPH simulation of acoustic waves: Effects of frequency, sound pressure, and particle spacing, *Math. Probl. Eng.* (2015) 348314.
- [44] G.R. Liu, M.B. Liu, Smoothed Particle Hydrodynamics –A Meshfree Particle Method, World Scientific, 2003.
- [45] Z.C. He, G.R. Liu, Z.H. Zhong, G.Y. Zhang, A.G. Cheng, A coupled ES-FEM/BEM method for fluid–structure interaction problems, *Eng. Anal. Bound. Elem.* 35 (2011) 140–147.
- [46] Z.C. He, G.R. Liu, Z.H. Zhong, S.C. Wu, G.Y. Zhang, A.G. Cheng, An edge-based smoothed finite element method (ES-FEM) for analyzing three-dimensional acoustic problems, *Comput. Methods Appl. Mech. Engrg.* 199 (2009) 20–33.
- [47] Z.C. He, G.R. Liu, Z.H. Zhong, G.Y. Zhang, A.G. Cheng, Coupled analysis of 3D structural-acoustic problems using the edge-based smoothed finite element method/finite element method, *Finite Elem. Anal. Des.* 46 (2010) 1114–1121.
- [48] Y.B. Chai, W. Li, Z.X. Gong, T.Y. Li, Hybrid smoothed finite element method for two-dimensional underwater acoustic scattering problems, *Ocean Eng.* 116 (2016) 129–141.
- [49] Y.B. Chai, W. Li, T.Y. Li, Z.X. Gong, X.Y. You, Analysis of underwater acoustic scattering problems using stable node-based smoothed finite element method, *Eng. Anal. Bound. Elem.* 72 (2016) 27–41.
- [50] W. Li, Y.B. Chai, M. Lei, T.Y. Li, Numerical investigation of the edge-based gradient smoothing technique for exterior helmholtz equation in two dimensions, *Comput. Struct.* 182 (2017) 149–164.
- [51] G. Wang, X.Y. Cui, Z.M. Liang, G.Y. Li, A coupled smoothed finite element method (S-FEM) for structural-acoustic analysis of shells, *Eng. Anal. Bound. Elem.* 61 (2015) 207–217.
- [52] G. Wang, X.Y. Cui, G.Y. Li, An element decomposition method for the Helmholtz equation, *Commun. Comput. Phys.* 20 (2016) 1258–1282.
- [53] G. Wang, X.Y. Cui, H. Feng, G.Y. Li, A stable node-based smoothed finite element method for acoustic problems, *Comput. Methods Appl. Mech. Engrg.* 297 (2015) 348–370.
- [54] Z.X. Gong, Y.B. Chai, W. Li, Coupled analysis of structural-acoustic problems using the cell-based smoothed three-node mindlin plate element, *Int. J. Comput. Methods* 13 (2016) 1640007.
- [55] H. Nguyen-Xuan, L.V. Tran, C.H. Thai, T. Nguyen-Thoi, Analysis of functionally graded plates by an efficient finite element method with node-based strain smoothing, *Thin-Walled Struct.* 54 (2012) 1–18.
- [56] X.Y. Cui, G.R. Liu, G.Y. Li, X. Zhao, T. Nguyen-Thoi, G.Y. Sun, A smoothed finite element method (SFEM) for linear and geometrically nonlinear analysis of plates and shells, *CMES Comput. Model. Eng. Sci.* 28 (2008) 109–125.
- [57] E. Li, Z.C. He, X. Xu, An edge-based smoothed tetrahedron finite element method (ES-T-FEM) for thermomechanical problems, *Int. J. Heat Mass Transfer* 66 (2013) 723–732.
- [58] B.Y. Xue, S.C. Wu, W.H. Zhang, G.R. Liu, A smoothed FEM (S-FEM) for heat transfer problems, *Int. J. Comput. Methods* 10 (2013) 1340001.
- [59] G.R. Liu, T. Nguyen-Thoi, H. Nguyen-Xuan, K.Y. Lam, A node-based smoothed finite element method (NS-FEM) for upper bound solutions to solid mechanics problems, *Comput. Struct.* 87 (2009) 14–26.
- [60] T. Nguyen-Thoi, H.C. Vu-Do, T. Rabczuk, H. Nguyen-Xuan, A node-based smoothed finite element method (NS-FEM) for upper bound solution to visco-elastoplastic analyses of solids using triangular and tetrahedral meshes, *Comput. Methods Appl. Mech. Engrg.* 199 (2010) 3005–3027.

- [61] G.R. Liu, T. Nguyen-Thoi, K.Y. Lam, An edge-based smoothed finite element method (ES-FEM) for static, free and forced vibration analyses of solids, *J. Sound Vib.* 320 (2009) 1100–1130.
- [62] G.R. Liu, T. Nguyen-Thoi, K.Y. Lam, A novel alpha finite element method (α FEM) for exact solution to mechanics problems using triangular and tetrahedral elements, *Comput. Methods Appl. Mech. Engrg.* 197 (2008) 3883–3897.
- [63] T. Nguyen-Thoi, P. Phung-Van, S. Nguyen-Hoang, Q. Lieu-Xuan, A coupled alpha-FEM for dynamic analyses of 2D fluid–solid interaction problems, *J. Comput. Appl. Math.* 271 (2014) 130–149.
- [64] N. Nguyen-Thanh, T. Rabczuk, H. Nguyen-Xuan, S. Bordas, An alternative alpha finite element method (A α FEM) for free and forced structural vibration using triangular meshes, *J. Comput. Appl. Math.* 233 (2010) 2112–2135.
- [65] C. Thai-Hoang, N. Nguyen-Thanh, H. Nguyen-Xuan, T. Rabczuk, An alternative alpha finite element method with discrete shear gap technique for analysis of laminated composite plates, *Appl. Math. Comput.* 217 (2011) 7324–7348.
- [66] N. Nguyen-Thanh, T. Rabczuk, H. Nguyen-Xuan, S. Bordas, An alternative alpha finite element method with discrete shear gap technique for analysis of isotropic Mindlin-Reissner plates, *Finite Elem. Anal. Des.* 47 (2011) 519–535.
- [67] H. Nguyen-Xuan, T. Rabczuk, N. Nguyen-Thanh, T. Nguyen-Thoi, S. Bordas, A node-based smoothed finite element method with stabilized discrete shear gap technique for analysis of Reissner–Mindlin plates, *Comput. Mech.* 46 (2010) 679–701.
- [68] T. Nguyen-Thoi, M.H. Nguyen-Thoi, T. Vo-Duy, N. Nguyen-Minh, Development of the cell-based smoothed discrete shear gap plate element (CS-FEM-DSG3) using three-node triangles, *Int. J. Comput. Methods* 12 (2015) 1540015.
- [69] M. Lyly, R. Stenberg, T. Viihinen, A stable bilinear element for the Reissner–Mindlin plate model, *Comput. Methods Appl. Mech. Engrg.* 110 (1993) 343–357.
- [70] N. Nguyen-Thanh, T. Rabczuk, H. Nguyen-Xuan, S. Bordas, A smoothed finite element method for shell analysis, *Comput. Methods Appl. Mech. Engrg.* 198 (2008) 165–177.
- [71] K.J. Bathe, E.N. Dvorkin, A four-node plate bending element based on Mindlin/Reissner plate theory and a mixed interpolation, *Internat. J. Numer. Methods Engrg.* 21 (1985) 367–383.
- [72] E.P. Kasper, R.L. Taylor, A mixed-enhanced strain method: Part I: Geometrically linear problems, *Comput. Struct.* 75 (2000) 237–250.
- [73] R.H. Macneal, R.L. Harder, A proposed standard set of problems to test finite element accuracy, *Finite Elem. Anal. Des.* 1 (1985) 3–20.
- [74] K.Y. Sze, D. Zhu, A quadratic assumed natural strain curved triangular shell element, *Comput. Methods Appl. Mech. Engrg.* 174 (1999) 57–71.
- [75] X.Y. Cui, G.R. Liu, G.Y. Li, G.Y. Zhang, G. Zheng, Analysis of plates and shells using an edge-based smoothed finite element method, *Comput. Mech.* 45 (2010) 141–156.
- [76] J.L. Batoz, K.J. Bathe, L.W. Ho, A study of three-node triangular plate bending elements, *Internat. J. Numer. Methods Engrg.* 15 (1980) 1771–1812.
- [77] A. Tessler, T.J.R. Hughes, A three-node mindlin plate element with improved transverse shear, *Comput. Methods Appl. Mech. Engrg.* 50 (1985) 71–101.
- [78] T. Nguyen-Thoi, P. Phung-Van, C. Thai-Hoang, H. Nguyen-Xuan, A cell-based smoothed discrete shear gap method (CS-DSG3) using triangular elements for static and free vibration analyses of shell structures, *Int. J. Mech. Sci.* 74 (2013) 32–45.
- [79] A.W. Leissa, Vibration of shell, Washington DC, NASA, SP-288, 1973.
- [80] Y.X. Zhang, Y.K. Cheung, W.J. Chen, Two refined non-conforming quadrilateral flat shell elements, *Internat. J. Numer. Methods Engrg.* 49 (2000) 355–382.
- [81] F. Tornabene, E. Viola, Vibration analysis of spherical structural elements using the GDQ method, *Comput. Math. Appl.* 53 (2007) 1538–1560.
- [82] L. Jiang, M.W. Chernuka, A simple four-noded corotational shell element for arbitrarily large rotations, *Comput. Struct.* 53 (1994) 1123–1132.
- [83] C.W.S. To, M.L. Liu, Hybrid strain based three node flat triangular shell elements–II. Numerical investigation of nonlinear problems, *Comput. Struct.* 54 (1995) 1057–1076.
- [84] C.Y. Chia, *Nonlinear Analysis of Plate*, McGraw-Hill, New York, 1980.